Effect of porosity on Curle's dipolar sources on an aerofoil in turbulent flow

Zamponi, R.; Satcunanathan, S.; Moreau, S.; Meinke, M.; Schröder, W.; Schram, C.

DOI
10.1016/j.jsv.2022.117353

Publication date
2023

Document Version
Final published version

Published in
Journal of Sound and Vibration

Journal of Sound and Vibration 542 (2023) 117353

Contents lists available at ScienceDirect

Journal of Sound and Vibration

journal homepage: www.elsevier.com/locate/jsvi

Effect of porosity on Curle's dipolar sources on an aerofoil in turbulent flow

R. Zamponi [a,b,*], S. Satcunanathan [c], S. Moreau [d], M. Meinke [c], W. Schröder [c], C. Schram [a]

[a] von Karman Institute for Fluid Dynamics, Waterlooses. 72, 1640 Sint-Genesius-Rode, Belgium
[b] Delft University of Technology, Kluyverweg 1, 2629 HS, Delft, The Netherlands
[c] RWTH Aachen University, Wüllnerstr. 5a, 52062 Aachen, Germany
[d] Université de Sherbrooke, Boul. de l'Université 2500, J1K 2R1 Sherbrooke, QC, Canada

ARTICLE INFO

Keywords:
Turbulence-interaction noise
Porous materials
Curle's analogy
Large-eddy simulations
Rod-aerofoil configuration

ABSTRACT

Integrating a porous material into the structure of an aerofoil constitutes a promising passive strategy for mitigating the noise from turbulence–body interactions that has been extensively explored in the past few decades. When a compact permeable body is considered in the aeroacoustic analogy derived by Curle to predict this noise source, a dipole associated with the non-zero unsteady Reynolds stresses appears on the surface in addition to the dipole linked to the pressure fluctuations. Nevertheless, the relative contribution of this source to the far-field noise radiated by a porous wing profile has not been clarified yet. The purpose of the current research work is twofold. On the one hand, it investigates the impact of porosity on the surface-pressure fluctuations of a thick aerofoil immersed in the wake of an upstream circular rod at a Mach number of 0.09. On the other hand, it quantifies the relevance of the Reynolds-stresses term on the surface as a sound-generation mechanism. The results from large-eddy simulations show that the porous treatment of the wing profile yields an attenuation of the unsteady-pressure peak, which is localised in the low-frequency range of the spectrum and is induced by the milder distortion of the incoming vortices. However, porosity is ineffective in breaking the spanwise coherence or in-phase behaviour of the surface-pressure fluctuations at the vortex-shedding frequency. The Reynolds-stresses term is found to be considerable in the stagnation region of the aerofoil, where the transpiration velocity is larger, and partly correlated with the unsteady surface pressure, suggesting constructive interference between the two terms. This results in a non-negligible contribution of this term to the far-field acoustic pressure emitted by the porous wing profile for observation angles near the stagnation streamline. The conclusions drawn in the present study eventually provide valuable insight into the design of innovative and efficient passive strategies to mitigate surface–turbulence interaction noise in industrial applications.

1. Introduction

The aerodynamic noise generated by the impingement of a turbulent flow on the surface of a wing represents a topic of active research that is related to numerous industrial applications. For instance, the noise due to the periodic interaction of the fan wakes

* Corresponding author at: von Karman Institute for Fluid Dynamics, Waterlooses. 72, 1640 Sint-Genesius-Rode, Belgium.
E-mail address: riccardo.zamponi@vki.ac.be (R. Zamponi).

https://doi.org/10.1016/j.jsv.2022.117353
Received 24 January 2022; Received in revised form 19 September 2022; Accepted 1 October 2022
Available online 6 October 2022

with the outlet guiding vanes (OGV) in modern turbofan engines [1] is receiving increasing attention due to the ever-larger bypass ratios adopted in their design, which, in turn, result in a decreased axial distance between fan and OGV and enhanced noise emissions [2]. Consequently, a significant effort has been put into mitigating this noise source, and one of the promising passive solutions proposed so far is to integrate a porous material into the structure of the wing or blade profile [3].

From a physical perspective, the turbulent eddies interacting with the leading edge of an aerofoil are subjected to a rapid distortion responsible for scattering part of their kinetic energy into sound [4], which is usually referred to as turbulence-interaction or leading-edge noise. A popular predictive method for the noise produced by this mechanism is based on the concept of aeroacoustic analogies. Lighthill [5] first demonstrated that the mechanisms accountable for the aerodynamic sound emitted by a turbulent flow could be represented, from the listener's point of view, by equivalent sources placed in a quiescent uniform medium. Such an approach has proved effective, especially for low Mach number applications. Lighthill's analogy was subsequently extended by Curle [6], who accounted for the presence of a body immersed in the flow and described the additional equivalent sources that arise due to turbulence-surface interactions as acoustic dipoles. These are associated with the reaction force that the body exerts on the surrounding fluid and are typically dominant at low Mach numbers. The topic of the present work is to investigate the influence of a porous material on the generation and propagation of such dipolar sources.

The idea of applying porosity as a passive noise-attenuation strategy has been considerably explored in the aeroacoustic community in the last three decades. The beneficial effects of the porous treatment of an aerofoil were first proved by Lee [7], who showed that the integration of a flow-permeable leading-edge insert into a helicopter blade resulted in a far-field noise reduction of up to 30% due to the suppression of the unsteady pressure on the blade surface. Next, Geyer et al. [8,9] investigated the influence of the porous properties on turbulence-interaction noise mitigation and concluded that higher values of static permeability yield more substantial attenuation at low frequencies but also increase at high frequencies due to the augmented surface roughness. The experimental dataset produced in that study was then exploited by Sarradj and Geyer [10] using symbolic regression tools to analyse the sensitivity of the different flow and material parameters on leading-edge noise. The results highlighted a dependency on the square of the turbulence intensity and from the fifth to the sixth power of the incoming mean-flow velocity. Furthermore, the ratio of the integral length scale of turbulence to the characteristic length of the porous structure, which is defined as the square root of the static permeability of the medium, was found to affect the far-field acoustic spectrum significantly.

When the entire chordwise extent of the aerofoil is made permeable to flow, a noticeable deterioration of the aerodynamic performance is expected, resulting in a decrease in the lift force and an increase in the drag force. The former is related to the pressure communication between the two sides of the aerofoil through the material's pores, whereas the latter is mainly linked to the higher surface roughness. The penalisation is thus more crucial at higher angles of incidence [8,11–13]. A possible technological solution for counteracting such effects is to limit the region of the wing profile where the flow can permeate to the leading edge [13–15] or integrate the porous medium in a rigid permeable exo-skeleton, including a solid centre plane to avoid cross-flow between the pressure and suction sides [16–18]. However, the centre plane should not extend over the full chord length to allow the incident velocity to penetrate the aerofoil surface in the stagnation region. This precaution is instrumental in achieving sound mitigation, as pointed out by Ocker et al. [19,20]. The solutions mentioned above make it possible to find a trade-off between turbulence-interaction noise reduction, aerodynamic-performance conservation, and structural-integrity preservation.

More recently, novel concepts for designing porous aerofoils based on non-uniform distributions of porosity have been proposed. Paruchuri et al. [21], Palleja-Cabre et al. [22], and Priddin et al. [23] investigated the leading-edge noise reduction achieved by flat plates with different extents of porous inserts and showed that a single row of holes located downstream of the stagnation point results in significant mitigation at low frequencies without increasing the noise emissions at high frequencies. Ayton et al. [24] found that smoothly varying chordwise porosity on a perforated flat plate can be beneficial for reducing trailing-edge noise thanks to the more significant destructive interference of the back-scattered field generated by the impermeable leading edge [25,26]. Moreover, Ayton et al. [27] observed that a spanwise-varying distribution of perforations on a flat plate could theoretically yield lower noise levels if compared with uniform porosity with a mechanism similar to that induced by leading-edge serrations. These studies demonstrate that the research on innovative porous materials is currently active, and there is room for further optimisation of the performance of such a passive noise-reduction strategy.

The present work represents the continuation of some research previously initiated by the authors. Specifically, Zamponi et al. [28] designed a porous aerofoil that integrates melamine foam into a permeable hard-plastic exo-skeleton shaped as a NACA-0024 profile. A centre plane prevents communication between the two sides of the model, while the surface is coated with a metallic wire mesh that guarantees a surface roughness with the desired quality. The aerofoil was placed in the wake generated by an upstream circular cylinder and compared with a solid baseline, highlighting a leading-edge noise decrease of up to 2 dB at low frequencies. In addition, large-eddy simulations (LES) for this experimental setup were carried out by Satcunanathan et al. [29] to shed additional light on the flow-field alterations caused by porosity. Both measurements and numerical computations were further analysed by Zamponi et al. [30,31], who identified the milder distortion experienced by the largest turbulent eddies as one of the prevalent noise-mitigation mechanisms related to the porous treatment of the wing profile. This link was subsequently confirmed by Tamaro et al. [32] with particle image velocimetry and acoustic far-field measurements. Furthermore, a model based on the rapid distortion theory (RDT) [33] was proposed by Zamponi et al. [34] to predict the changes in the turbulent velocity experienced by a porous body that interacts with prescribed incoming turbulence and interpret the experimental results. Such a semi-analytic method could lay the foundation for developing novel noise-prediction tools for porous aerofoils.

While the studies outlined above provide some insight into the attenuation of the distortion of incoming turbulence, the impact of porosity on Curle's dipolar sources has not been addressed. Moreover, the integral solution of Lighthill/Curle's analogy assumes no-slip and no-penetration boundary conditions at the surface of the body surrounded by turbulence. This assumption is no longer

valid when the surface is permeable, so additional equivalent-source terms appear in the derivation. A better understanding of how all the equivalent sources are affected would be instrumental in designing more effective noise-reduction techniques and constitutes the objective pursued in the present research. The information on the flow field extracted from the LES data produced and validated in the previous works is considered here. The outcome of this investigation will eventually provide helpful insight into the design of innovative and more effective porous treatments.

The remainder of the paper is structured as follows. A recap of the derivations of Curle's analogy is reported in Section 2. Section 3 discusses the computational methodology and briefly describes the model equations for the porous media and the turbulent-flow prediction. In Section 4, the numerical setup, flow conditions, and data processing settings are described. Section 5 presents the achieved results, addressing the role of porosity on Curle's dipolar sources on the aerofoil surface. Finally, conclusions are drawn in Section 6.

2. Theory: Curle's analogy for a porous body

Upon definition of a thermodynamic reference state indicated by the density ρ_0 and pressure p_0 that refer to a uniform medium at rest, the propagation of density perturbations $\rho' = \rho - \rho_0$ at the speed of sound $c_0 = \sqrt{(\partial p/\partial \rho)_s}$, s being the entropy, in a homogeneous acoustic medium is described by Lighthill's analogy [5] as

$$\frac{\partial^2 \rho'}{\partial t^2} - c_0^2 \frac{\partial^2 \rho'}{\partial {x_\mathrm{i}}^2} = \frac{\partial^2 T_\mathrm{ij}}{\partial x_\mathrm{i} \partial x_\mathrm{j}}, \tag{1}$$

where $T_\mathrm{ij} = \rho u_\mathrm{i} u_\mathrm{j} - \tau_\mathrm{ij} + (p' - c_0^2 \rho') \delta_\mathrm{ij}$ is denoted as Lighthill's stress tensor [5], which accounts for the sound produced by Reynolds stresses $\rho u_\mathrm{i} u_\mathrm{j}$, $\boldsymbol{u}$ being the flow velocity, viscous stresses τ_ij, and non-isentropic processes. Here, δ is the Dirac delta function. For high Reynolds numbers, the contribution of the viscous forces can be neglected and with the assumption of incompressible and isentropic flow, Lighthill's stress tensor can be approximated as $T_\mathrm{ij} \approx \rho_0 u_\mathrm{i} u_\mathrm{j}$.

In the presence of a stationary surface S in the control domain V, the solution of Eq. (1) using the Green's function approach [35] can be expressed for a listener located at position $\boldsymbol{x}$ in space at time t and a source placed at position $\boldsymbol{y}$ in space at emission time τ by

$$c_0^2 \rho'(\boldsymbol{x}, t) = \int_{-\infty}^{t} \iiint_V \frac{\partial^2 T_\mathrm{ij}}{\partial y_\mathrm{i} \partial y_\mathrm{j}} G \, \mathrm{d}V \, \mathrm{d}\tau + c_0^2 \int_{-\infty}^{t} \iint_S \left(\rho' \frac{\partial G}{\partial y_\mathrm{i}} - G \frac{\partial \rho'}{\partial y_\mathrm{i}} \right) n_\mathrm{i} \, \mathrm{d}S \, \mathrm{d}\tau, \tag{2}$$

where $\boldsymbol{n}$ is the outward-pointing normal on S and G is the Green's function [36]. The first term on the right-hand side of the equation indicates the incident acoustic field, whereas the second one represents the sound scattered by the surface. The incident-field integral can be reformulated by performing integration by parts, and the partial derivatives can be moved from the source to the Green's function. Using the divergence theorem and imposing the momentum conservation law [35], Eq. (2) becomes

$$\begin{aligned} p^*(\boldsymbol{x}, t) = & \int_{-\infty}^{t} \iiint_V \frac{\partial^2 G}{\partial y_\mathrm{i} \partial y_\mathrm{j}} T_\mathrm{ij} \, \mathrm{d}V \, \mathrm{d}\tau \\ & + c_0^2 \int_{-\infty}^{t} \iint_S \left[G \frac{\partial \rho u_\mathrm{i}}{\partial \tau} + \left(p' \delta_\mathrm{ij} + \rho u_\mathrm{i} u_\mathrm{j} \right) \frac{\partial G}{\partial y_\mathrm{i}} \right] n_\mathrm{i} \, \mathrm{d}S \, \mathrm{d}\tau \end{aligned} \tag{3}$$

where $p^* \equiv c_0^2 \rho'$ denotes the acoustic pressure at the listener position. The viscous stresses have been neglected with regard to the pressure fluctuations and Reynolds stresses in the last integral, owing to the assumed large Reynolds number. If the body is impermeable, the velocity u_i on the surface is zero and the terms $\partial \rho u_\mathrm{i}/\partial \tau$ and $\rho u_\mathrm{i} u_\mathrm{j}$ in the surface integral vanish. Conversely, for a porous surface, the flow penetration within the inner volume of the body is permitted, and these two terms have to be retained.

Subsequently, the application of the free-field Green's function

$$G_0(\boldsymbol{x}, t | \boldsymbol{y}, \tau) = \frac{\delta(t - \tau - \|\boldsymbol{x} - \boldsymbol{y}\|/c_0)}{4\pi \|\boldsymbol{x} - \boldsymbol{y}\|} \tag{4}$$

makes it possible to carry out the time integrals in Eq. (3) [6], yielding

$$\begin{aligned} p^*(\boldsymbol{x}, t) = & \frac{\partial^2}{\partial x_\mathrm{i} \partial x_\mathrm{j}} \iiint_V \left[\frac{T_\mathrm{ij}}{4\pi \|\boldsymbol{x} - \boldsymbol{y}\|} \right]_{t=\hat{\tau}} \mathrm{d}V \\ & - \frac{\partial}{\partial x_\mathrm{i}} \iint_S \left[\frac{p' \delta_\mathrm{ij} + \rho u_\mathrm{i} u_\mathrm{j}}{4\pi \|\boldsymbol{x} - \boldsymbol{y}\|} \right]_{t=\hat{\tau}} n_\mathrm{j} \, \mathrm{d}S + \iint_S \left[\frac{\partial \rho u_\mathrm{j}}{\partial \tau} \frac{1}{4\pi \|\boldsymbol{x} - \boldsymbol{y}\|} \right]_{t=\hat{\tau}} n_\mathrm{j} \, \mathrm{d}S, \end{aligned} \tag{5}$$

where $\hat{\tau} = t - \|\boldsymbol{x} - \boldsymbol{y}\|/c_0$ is the retarded time at which the source terms are evaluated. Furthermore, if the body is assumed to be acoustically compact, i.e. the size of the source region is small compared with the acoustic wavelength λ, the variation of $\hat{\tau}$ over the surface can be neglected, and the square brackets can be moved out of the integral. Additionally, in the geometric far-field, namely at a distance much greater than the characteristic dimension of the body, the term $4\pi \|\boldsymbol{x} - \boldsymbol{y}\|$ can be approximated to $4\pi r$, r being the averaged distance between the source region and listener.

The outcome of the analysis is that multiple terms contribute to the radiated sound when a permeable or rigid-permeable surface is immersed in a turbulent flow. The first volume integral in the right-hand side of Eq. (5) is the usual quadrupolar term of Curle's integral solution. By using the relation [35]

$$\frac{\partial f(\hat{\tau})}{\partial x_\mathrm{i}} = \left[\frac{\partial f(\tau)}{\partial \tau} \right]_{\tau=\hat{\tau}} \frac{\partial \hat{\tau}}{\partial x_\mathrm{i}} = - \frac{(x_\mathrm{i} - y_\mathrm{i})}{\|\boldsymbol{x} - \boldsymbol{y}\| c_0} \left[\frac{\partial f(\tau)}{\partial \tau} \right]_{\tau=\hat{\tau}} \tag{6}$$

and dropping the terms of order $1/r^2$ and $1/r^3$ that can be considered negligible in the geometric far-field, the quadrupolar term becomes

$$p^*_{\text{quadrupole}}(\boldsymbol{x},t) \approx \frac{x_\text{i}x_\text{j}}{4\pi\, c_0^2 r^3}\left[\iiint_V \frac{\partial^2 T_\text{ij}}{\partial\tau^2}\,\mathrm{d}V\right]_{\tau=\hat{\tau}}. \tag{7}$$

The first surface integral in the right-hand side of Eq. (5) is the dipolar term, which accounts for the surface loading and typically dominates over the quadrupolar one for low Mach number applications and acoustically compact source regions. From Eq. (6) and considering the far-field approximation, it follows that

$$p^*_{\text{dipole}}(\boldsymbol{x},t) \approx \frac{x_\text{i}}{4\pi\, c_0 r^2}\left[\iint_S \frac{\partial\left(p'\delta_\text{ij}+\rho u_\text{i}u_\text{j}\right)}{\partial\tau}\,n_\text{j}\,\mathrm{d}S\right]_{\tau=\hat{\tau}}. \tag{8}$$

Eq. (8) states that the distribution of dipoles representing fluctuating forces acting on the fluid from the porous body is produced by two components, one linked to the surface-pressure fluctuations, denoted as the *unsteady-pressure term*, and the other one to the variation of Reynolds stresses on the surface, indicated as the *Reynolds-stresses term*. For an impermeable body, only the former is non-zero, whereas the latter appears solely when the airflow can penetrate the inner volume of the body, i.e. with a porous material. In Section 5, the contribution to the far-field acoustic pressure provided by these terms will be evaluated separately.

Finally, the second surface integral in the right-hand side of Eq. (5) is the monopolar term, which is related to the rate of mass flux across the body surface and can be expressed as

$$p^*_{\text{monopole}}(\boldsymbol{x},t) \approx \frac{1}{4\pi\, r}\left[\iint_S \frac{\partial\rho u_\text{j}}{\partial\tau}\,n_\text{j}\,\mathrm{d}S\right]_{\tau=\hat{\tau}}. \tag{9}$$

By exploiting the reciprocity principle according to which $\partial/\partial\tau = -\partial/\partial t$, the time derivative can be moved out of the surface integral, and this term is null by the conservation of mass. However, it is worth pointing out that when the assumption of acoustic compactness is not verified, i.e. the variation of retarded time over the surface is not negligible anymore, the monopolar term may contribute to the overall sound produced by a porous body immersed in a turbulent flow. This equivalent source would have a dipolar efficiency at leading order due to the destructive interference between the surface patches where the flow enters and leaves the body. Studying this noise source will undoubtedly be a topic for future work.

3. Computational methodology

As introduced in Section 1, the turbulent-flow field is predicted using an LES based on the compressible Navier–Stokes equations. These equations are equally valid inside the porous material and can be employed to fully resolve the flow through the porous micro-structures, though being computationally challenging for various reasons. On the one hand, this requires the complex pore morphology to be available, e.g. with a computerised tomography scan, which is often not the case. On the other hand, the requirement on the grid resolution would be severe due to the tiny pore structures being typically smaller than the smallest length scale of the turbulence.

Only the integral effects or flow alterations in the outer region by a porous treatment are often of interest. A well-established approach is to neglect the micro-scale introduced by the material's pores by the method of volume averaging [37,38]. This procedure replaces the distinct fluid and solid regions in the porous material with a locally homogeneous medium with continuously varying field variables. These are then governed by the volume-averaged Navier–Stokes equations (VANS) augmented by closure terms, which emerge from the spatial filtering process and account for sub-grid effects. For more details, the reader is referred to Satcunanathan et al. [29].

In the subsequent brief consideration, let Ω be the total simulation domain, $\Omega_f = \{\boldsymbol{x} \in \Omega \mid \varphi(\boldsymbol{x}) = 1\}$ the fluid region, $\Omega_p = \{\boldsymbol{x} \in \Omega \mid \varphi(\boldsymbol{x}) < 1\}$ the porous region with $\Omega_g \cap \Omega_p = \emptyset$, and $\Gamma = \partial\Omega_f \cap \Omega_p$ the fluid-porous interface (see Fig. 1(b)). The porosity φ is the volume ratio of the open pores to the total volume of the porous material and is equal to 1 in the free fluid. Using the symbol $\langle\ \rangle$ to denote the intrinsic average and $\langle\ \rangle_F$ the Favre average, the conservation of mass, momentum, and energy in non-dimensional integral form formulated for an arbitrary control volume V reads

$$\frac{\mathrm{d}}{\mathrm{d}t}\int_{V\in\Omega} \boldsymbol{Q}\,\mathrm{d}V + \oint_{\partial V\in\Omega}\left(\boldsymbol{H}^\text{inv}-\boldsymbol{H}^\text{vis}\right)\cdot\boldsymbol{n}\,\mathrm{d}S + \int_{V\in\Omega}\left(\frac{1}{\varphi}\boldsymbol{H}^\text{inv}\cdot\nabla\varphi+\boldsymbol{S}\right)\mathrm{d}V = 0, \tag{10}$$

where $\boldsymbol{Q} = \left[\langle\rho\rangle, \langle\rho\rangle\langle\boldsymbol{u}\rangle_F, \langle\rho\rangle\langle E\rangle_F\right]^T$ is the vector of spatially-averaged conservative variables. The inviscid and viscous flux tensors are given by

$$\boldsymbol{H}^\text{inv}-\boldsymbol{H}^\text{vis} = \begin{bmatrix} \langle\rho\rangle\langle\boldsymbol{u}\rangle_F \\ \langle\rho\rangle\langle\boldsymbol{u}\rangle_F\otimes\langle\boldsymbol{u}\rangle_F + \langle p\rangle\boldsymbol{I} \\ \langle\rho\rangle\langle E\rangle_F\langle\boldsymbol{u}\rangle_F + \langle p\rangle\langle\boldsymbol{u}\rangle_F \end{bmatrix} - \frac{1}{Re}\begin{bmatrix} 0 \\ \langle\boldsymbol{\tau}\rangle_F \\ \langle\boldsymbol{\tau}\rangle_F\cdot\langle\boldsymbol{u}\rangle_F + \frac{1}{Pr}\langle\boldsymbol{q}\rangle \end{bmatrix}. \tag{11}$$

The quantities E, $\boldsymbol{q}$, $\boldsymbol{I}$, Re, and Pr denote the total energy, heat-flux vector, unit tensor, Reynolds number, and Prandtl number, respectively. The first two integrals in Eq. (10) are formally identical to the equations solved in a monotone integrated LES (MILES)

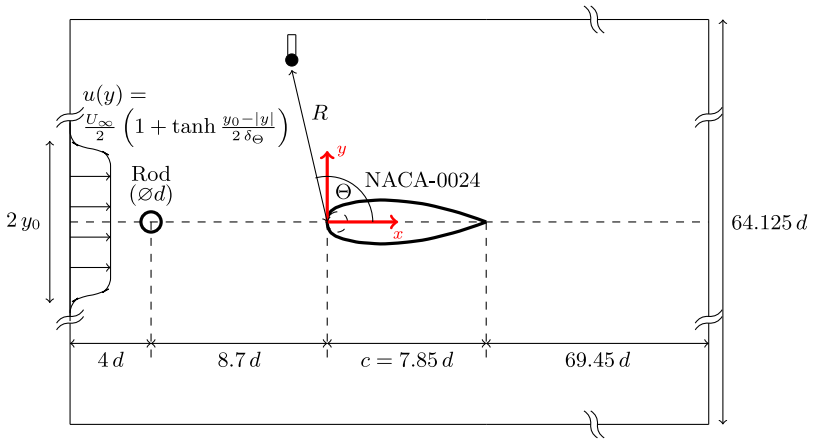

(a)

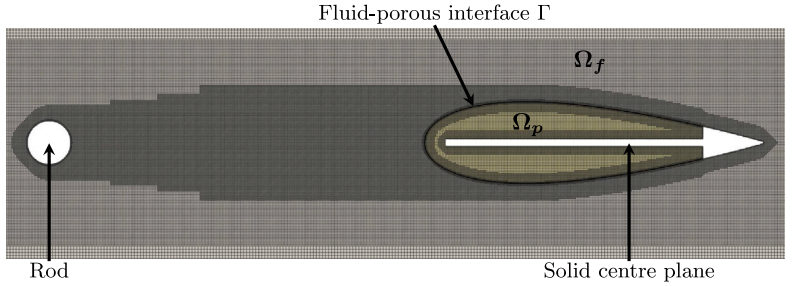

(b)

Fig. 1. (*a*) 2D sketch of the computational domain. The observer is located at a distance of R from the leading edge. The angle Θ is measured from the positive x-axis. (*b*) Close-up view of a locally refined Cartesian grid around the rod and porous aerofoil (only every other grid line is plotted to ease the visualisation). The part of the wing profile made of melamine foam, i.e. the Ω_p region, is indicated in yellow. (For interpretation of the references to colour in this figure legend, the reader is referred to the web version of this article.)

context for $\varphi = 1$, where no explicit modelling of the sub-grid scale is used. The first term in the last integral is the contribution of the inviscid flux vector at the fluid-porous interface $\boldsymbol{H}^{int} = \boldsymbol{H}^{\text{inv}} - \langle p\rangle \boldsymbol{I}$. The surface-filter term

$$\boldsymbol{S} = \begin{cases} \left[0, \boldsymbol{F}/\varphi, 0\right]^T, & \boldsymbol{x} \in \Omega_p \\ \boldsymbol{0}^T, & \boldsymbol{x} \in \Omega_f \end{cases} \tag{12}$$

contains the porous-drag vector $\boldsymbol{F}$ that is closed through the Darcy–Forchheimer model [39,40], expressed for a homogeneous and isotropic porous medium as

$$\boldsymbol{F} = \underbrace{\frac{1}{Re_k\sqrt{Da}}\varphi\mu\langle\boldsymbol{u}\rangle_F}_{\text{Darcy}} + \underbrace{\frac{1}{\sqrt{Da}}\varphi^2 c_f\langle\rho\rangle|\langle\boldsymbol{u}\rangle_F|\langle\boldsymbol{u}\rangle_F}_{\text{Forchheimer}}. \tag{13}$$

The permeability Reynolds number, $Re_k = Re\sqrt{Da}$, is computed with $d_p \sim \sqrt{k}$ as the length scale, which is a measure for the effective pore diameter, while the Darcy number, Da, is defined as $Da = k/L^2$, L being a reference length. The Darcy–Forchheimer model in Eq. (13), together with Eq. (10), characterises the porous medium in terms of the porosity, φ, static permeability, k, and Forchheimer coefficient, c_f, and assumes the porous frame to be rigid, neglecting coupling effects due to elasticity as well as thermal effects. The equations are solved by a finite-volume method, which has been discretised in space by an advective upstream splitting method (AUSM) for the inviscid fluxes and a centred discretisation of the viscous fluxes. The semi-discretised equations are advanced in time by a five-stage explicit Runge–Kutta scheme. The overall scheme is second-order accurate in space and time, while the LES is based on the MILES ansatz. The equations are discretised on a locally refined, unstructured, Cartesian mesh with a fully conservative cut-cell approach for the wall boundaries [41].

Eq. (10) is valid in the pure fluid and porous regions, but assumptions made during the derivation are violated across the fluid-porous interface Γ. Additionally, the sudden change of φ across Γ makes the equations stiff. It can be shown that the arising

Dirac-shaped source terms can be equally replaced by jumps of the flow variables across an idealised sharp immersed fluid-porous interface on a non-interface fitted Cartesian mesh. In such a fluid-porous cut cell, the volume-weighted average of the state vector $\boldsymbol{Q} = \varphi\, \boldsymbol{Q}_f + (1-\varphi)\, \boldsymbol{Q}_p$ is integrated in time, preventing the emergence of small cells, which may pose stringent time-step constraints for hyperbolic solvers. In this case, the flow variables on the porous surface correspond to $\boldsymbol{Q}_f$ of the respective cut cell. For a more detailed description of the method, the reader is referred to [29].

4. Computational setup

The observations and outcome of the theoretical analysis in Section 2 will be applied to the existing numerical simulation data of a rod-aerofoil configuration being already the subject of previous leading-edge noise investigations [29,30].

4.1. Rod-aerofoil configuration

In the rod-aerofoil arrangement, conceived by Jacob et al. [42] as an aeroacoustic benchmark problem, the wing profile undergoes a broadband perturbation dominated by a specific shedding frequency, similar to several aeronautical applications [43]. In the discussion below, all lengths are given as multiple of the cylindrical rod diameter $d = 0.02\,\mathrm{m}$, which is located $8.2\,d$ upstream of a two-dimensional NACA-0024 profile with a chord length of $c = 7.85\,d$ and a leading-edge radius of $r_{LE} = 0.5\,d$ at 0° angle of attack. The rather thick aerofoil will cause a considerable displacement and distortion of the mean flow, the implications of which have been formerly analysed in [30].

In Fig. 1(a), the overall arrangement is symmetrical with respect to the streamwise direction. The coordinate system used in the present study is defined as follows: the x-axis is aligned with the streamwise direction, the y-axis is aligned with the upwash direction, and the z-axis is aligned in the spanwise direction to form a right-handed coordinate system with the origin at the leading edge of the wing profile. The rod and aerofoil are placed in the potential core of a plane jet of Mach number $M = 0.09$ and width $7.5\,d$. At the inlet, a tangent hyperbolic velocity profile with super-imposed synthetic eddies [44] generating a 1% turbulence intensity is prescribed to simulate realistic atmospheric or wind tunnel disturbances of the incident flow. The jet shear-layer thickness is initialised to $\delta_\Theta/d = 0.04$. To avoid the emergence of large Kelvin–Helmholtz type roll-ups that might contaminate the flow around the aerofoil, a shear layer break-up was induced using the jet shear-layer forcing proposed by Bogey and Bailly [45].

The Reynolds numbers based on the rod diameter and on the wing-profile chord are $Re_d = 4.0 \times 10^4$ and $Re_c = 3.14 \times 10^5$, which correspond to a free-stream flow velocity of $30\,\mathrm{m\,s^{-1}}$. Under these conditions, a turbulent wake with embedded shed vortices will impinge on the aerofoil leading edge.

4.2. Solid and porous aerofoil models

Simulations of two configurations, differing in the material of the NACA-0024 profile, have been conducted. The first is a classical solid aerofoil where the no-slip boundary condition is satisfied on the surface. The second is a wing profile whose bulk volume is assumed to be porous, as indicated in Fig. 1(b). An impermeable centre plane preventing the cross-flow between the upper and lower sides of the aerofoil (see Section 1) extends from one leading-edge radius downstream of the stagnation point to the trailing edge, allowing for the flow penetration into the inner volume in the stagnation region.

In the present study, the porous medium is assumed to be melamine foam with homogeneous and isotropic material properties as proposed in [28]. The characterisation required to set up the model in Eq. (13) is described by Satcunanathan et al. [46], and the corresponding parameters are $\varphi = 0.986$, $Da = 5.3 \times 10^{-6}$, and $c_f = 0$. For the computation of the Darcy number, the rod diameter is considered the reference length. As a consequence, $Re_k = 92$. In the fluid Ω_f and porous Ω_p regions, Eq. (10) is solved with the surface-filter terms from Eq. (12) and with $\boldsymbol{H}^{int}$ neglected. Instead, both domains are matched at the interface in the respective cut-cells by means of the jump conditions.

4.3. Computational domain

The computational domain extends $90\,d \times 64\,d \times \pi\,d$ in the streamwise, upwash, and spanwise directions, respectively, resulting in 186 million mesh points for the solid configuration and 206 million grid points for the porous one. As depicted in Fig. 1(b), the grid is locally refined around solid boundaries and in the fluid-porous interface Γ around the aerofoil and gradually coarsened in the outer field. The local grid spacing is here given by $\Delta_r = 144/2^{R_L}$, where R_L is the refinement level that ranges from 11 to 15, i.e. the smallest cell size is $4.39 \times 10^{-3}\,d$. Finally, periodic boundary conditions are imposed in the spanwise direction, and constant atmospheric pressure is enforced on the far-field boundaries with a sponge treatment at the out-flow boundary to damp spurious waves.

4.4. LES data processing

The current investigation features the processing of the time signals of pressure, velocity, and density fluctuations over the aerofoil surface and in the upstream flow. Basic expressions that will be applied to the simulated data are briefly defined in this section.

4.4.1. Flow-field and surface quantities

After the transient, the turbulent-flow field is time-averaged to calculate the related statistics at each domain location. These values are processed at a sampling frequency of $f_s = 25.6\,\text{kHz}$ for a total of $T_s U_\infty/d = 78$ time units, which correspond to approximately 15.6 shedding cycles at a Strouhal number of $St = 0.2$ based on the rod diameter and free-stream velocity, to reach statistical convergence. The averaged and root-mean-square (r.m.s.) velocities extracted along the stagnation streamline of the wing profile have been compared with hot-wire measurements in [30] to validate the numerical data.

The frequency-domain quantities employed in the subsequent sections are computed by the Welch periodogram method [47], using Hanning windows of blocks of 2^9 samples with 75% overlap, thus providing a frequency resolution of approximately 48 Hz. Among these, the normalised magnitude-squared spatial coherence between the reference time signal q_0 and generic time signal q is defined as

$$\gamma^2_{q_0 q}(f) = \frac{|\boldsymbol{\Phi}_{q_0 q}(f)|^2}{\boldsymbol{\Phi}_{q_0 q_0}(f)\,\boldsymbol{\Phi}_{qq}(f)}, \tag{14}$$

where $\boldsymbol{\Phi}_{q_0 q_0}$ denotes the power spectral density of q_0, while $\boldsymbol{\Phi}_{q_0 q}$ indicates the cross-spectral density between q_0 and q. From the latter, the phase difference between the two signals can be computed as

$$\phi_{q_0 q}(f) = \text{Im}\left[\boldsymbol{\Phi}_{q_0 q}(f)\right]. \tag{15}$$

4.4.2. Integration of Curle's dipolar sources

The instantaneous pressure, density, and velocity data along the surface of the solid and porous aerofoils are considered for computing the dipolar sources derived in Eq. (8) and evaluating the resulting radiated far-field acoustic pressure. However, the proposed formulation is only valid for acoustically-compact source regions, for which Curle's analogy has proved to deliver consistent sound-pressure level estimations [48]. This limitation does not allow integrating the equivalent dipoles over the whole surface of the wing profile since it is not acoustically compact in the entire frequency range of interest. Hence, the focus of the current investigation is not to evaluate the total noise emitted by the aerofoil but rather find an estimate for the dominant part of the surface contribution.

To pursue this objective, several chordwise-varying squared areas along the aerofoil span are taken as integration regions. The size of each patch is chosen to be acoustically compact, with $L = 0.25\,r_{LE}$. This value satisfies the condition $L \ll \lambda_{\max}$, where $\lambda_{\max}$ is the wavelength associated with the maximum analysed frequency, namely $f_{\max} = f_s/2 = 12.8\,\text{kHz}$. Finally, for calculating the integrals in Eq. (8), time derivatives are approximated with a finite-difference method, using a second-order upwind scheme.

5. Results and discussion

This section presents the results of the analysis of Curle's dipolar sources. First, the effect of porosity on the pressure fluctuations on the surface of the aerofoil is evaluated. Second, the impact of the noise sources produced by the non-zero Reynolds stresses on the porous surface and their correlation with the unsteady-pressure term are discussed.

5.1. Unsteady-pressure term

As shown in Section 2, the interaction of the upstream turbulent flow shed by the circular rod with the aerofoil induces unsteady pressures on its surface. Figs. 2(a) and 2(b) depict the contours of the r.m.s. surface-pressure fluctuations for the solid and porous cases, respectively. The values are normalised by the free-stream dynamic pressure. Interestingly, the region with the highest pressure amplitudes is not located at the leading edge but slightly downstream of it. For the impermeable aerofoil (Fig. 2(a)), the largest r.m.s. pressure fluctuations appear to be at a chordwise location of $x/r_{LE} \approx 0.47$. One possible reason behind this downstream displacement could be attributed to the significant thickness of the NACA-0024 profile. Indeed, the leading edge of such an aerofoil does not constitute a sharp geometric singularity. The turbulent structures advected towards the stagnation region by the mean-flow field are subjected to a strong acceleration in the area of the largest streamline curvature and impinge on the surface at higher velocities and more downstream locations [49].

Moving the attention to the porous configuration, the possibility for the flow to penetrate the body is seen to result in an attenuation of the peak amplitude (Fig. 2(b)), which is spread over a larger region. The mitigation effect of porosity on the unsteady pressure is likely responsible for the far-field noise reduction previously analysed in [28–30,32]. The trends discussed so far are better visualised in Fig. 2(c), which depicts the r.m.s. surface-pressure fluctuation profiles of the aerofoils averaged over the span. The attenuation in the unsteady-pressure peak at $x/c \approx 0.03$, corresponding to $x/r_{LE} \approx 0.47$, amounts to about 20%. Downstream of the peak region, the surface-pressure fluctuations decay faster for the solid configuration than for the porous one up to $x/c \approx 0.4$, maintaining relatively steady r.m.s. values for the remaining part of the wing profile.

The effect of porosity on the spanwise spatial coherence $\gamma^2_{p'_0 p'}$ of the unsteady-pressure term between the midspan of the aerofoil ($z/r_{LE} = 0$) and spanwise-varying locations is shown in Fig. 3. This quantity is a measure of the acoustic efficiency of a noise source [50]. Two streamwise locations are considered for the computation of $\gamma^2_{p'_0 p'}$, namely $x/r_{LE} = 0$, i.e. the leading edge, and $x/r_{LE} = 0.47$, i.e. the position where the largest pressure fluctuations occur. Since periodic boundary conditions have been used in the prediction of the turbulent field (see Section 3), the spatial-coherence values are meaningful only for separation distances less than half the simulated span, which corresponds to approximately $3.2\,r_{LE}$ [29]. The results are presented as a function of the Strouhal number St based on the cylindrical rod diameter and the free-stream velocity.

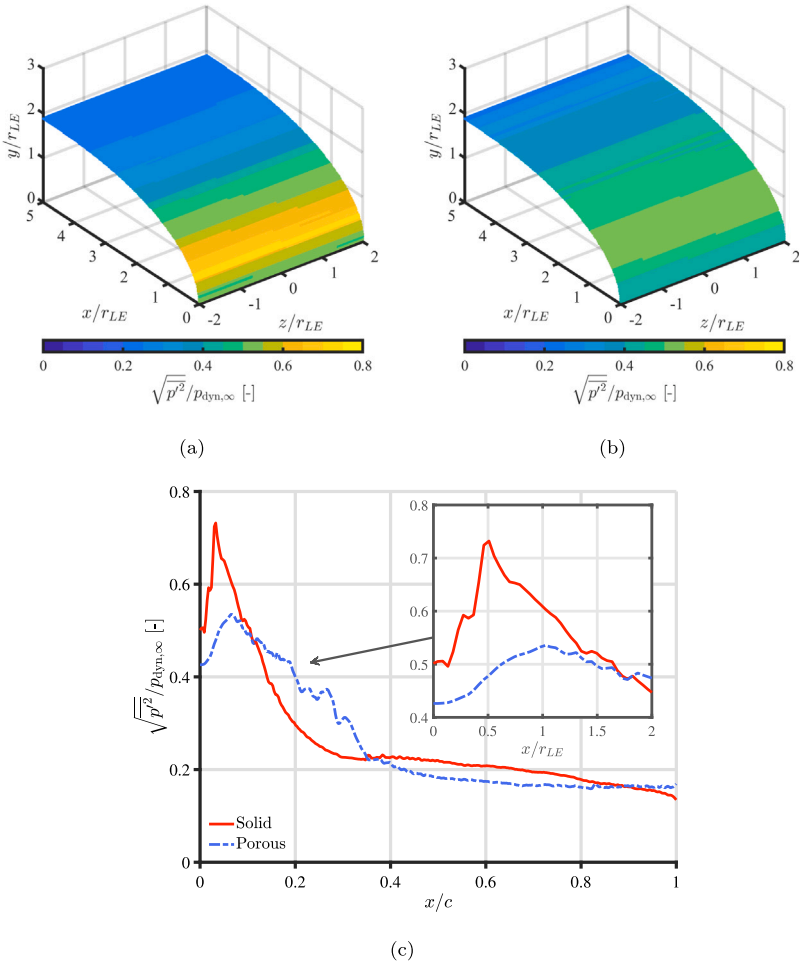

Fig. 2. R.m.s. pressure-fluctuations contours on the surface of the (*a*) solid and (*b*) porous aerofoils made dimensionless by the free-stream dynamic pressure $p_{\mathrm{dyn},\infty}$. (*c*) R.m.s. pressure fluctuations on the surface of the aerofoils averaged over the span.

At the aerofoil leading edge (Fig. 3(a)), porosity appears to have a minor impact on the spanwise coherence. For both solid and porous configurations, $\gamma^2_{p'_0p'}$ is maximum for lower St (due to the effect of the mean flow) and z and rapidly decreases with increasing frequency. The only exception occurs at the Strouhal number linked to the fluctuating drag, i.e. $St \approx 0.4$, where unsteady pressures on the impermeable wing-profile surface remain partly coherent over a distance of two leading-edge radii from the midspan. The same trend is not found for the porous case. Moreover, the contours exhibit no prominent peak associated with the vortex shedding, which is, instead, clearly visible at the location of largest r.m.s. pressure fluctuations (Fig. 3(b)). Indeed, the spanwise spatial coherence of the unsteady pressure at $St = 0.2$ remains high over the whole span for both aerofoils at this position. The integration of porosity only results in a marginal attenuation of this quantity but decreases the amplitude of the $\gamma^2_{p'_0p'}$ peaks in the range $0.4 < St < 0.8$ for $z/r_{LE} < 2$.

Interestingly, a slight shift of the shedding frequency towards lower Strouhal numbers occurs for the porous wing profile. This trend agrees with previous observations conducted on equivalent NACA-0024 profiles [32] and may be related to a different blockage exerted by the aerofoil due to the wider boundary layer developed over the flow-permeable surface [3]. Such a phenomenon has also been observed for porous cylinders arranged in a tandem configuration [51,52]. The extraction of the spanwise spatial-coherence contours in Figs. 3(a) and 3(b) interpolated for $0.195 < St < 0.205$ allows clarifying this tendency and is illustrated in Fig. 4. While $\gamma^2_{p'_0p'}$ decays over a relatively short distance for the three St under consideration at the leading edge (Fig. 4(a)), reaching values below 0.5 within $1\,r_{LE}$ from midspan, it remains above 0.8 for the entire span at $x/r_{LE} = 0.47$ for both aerofoils (Fig. 4(b)). At the latter position, the possibility of the flow permeating the wing profile results in a reduction of up to 10% in the spatial coherence. In this case, the mitigation becomes more significant for the higher Strouhal number, hinting at the aforementioned shift of the vortex-shedding peak, whereas $\gamma^2_{p'_0p'}$ is the same for $St = 0.195$ and $St = 0.2$.

Additionally, the unsteady pressures on the surface of the aerofoils maintain a high degree of correlation with those at the location where the largest fluctuations occur along the chord. Fig. 5 compares the spatial coherence between the solid and porous

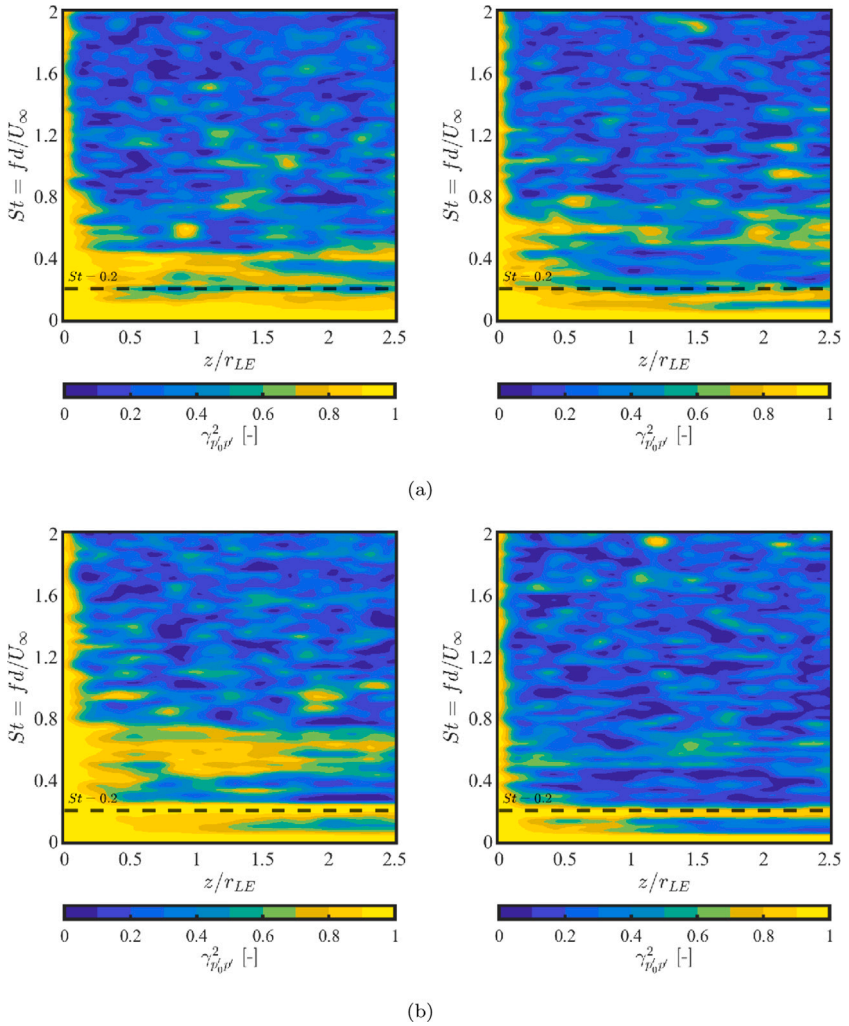

Fig. 3. Spanwise spatial-coherence contours of the pressure fluctuations on the surface of the solid (on the left) and porous (on the right) aerofoils computed at (*a*) $x/r_{LE} = 0$ and (*b*) $x/r_{LE} = 0.47$. The reference is set at the midspan location ($z/r_{LE} = 0$). The dashed line indicates the Strouhal number corresponding to the vortex-shedding peak.

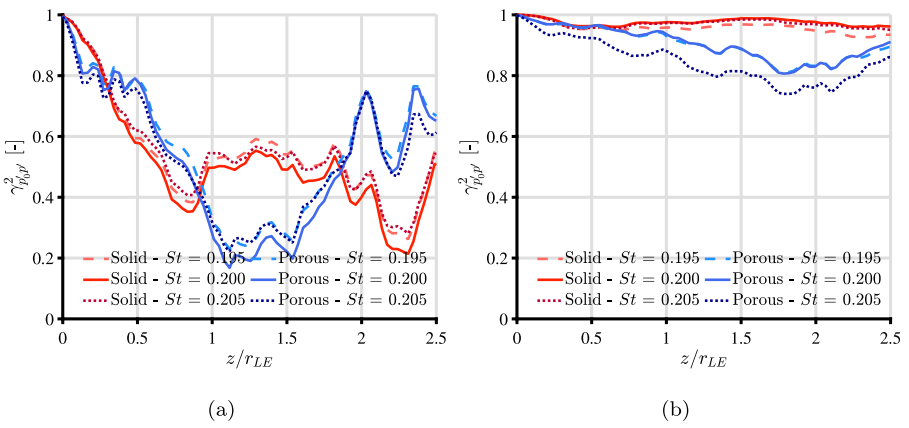

Fig. 4. Spanwise spatial-coherence profiles of the pressure fluctuations on the surface of the solid and porous aerofoils computed at (*a*) $x/r_{LE} = 0$ and (*b*) $x/r_{LE} = 0.47$ for different interpolated Strouhal numbers in the vicinity of the vortex-shedding frequency peak. The reference is set at the midspan location ($z/r_{LE} = 0$).

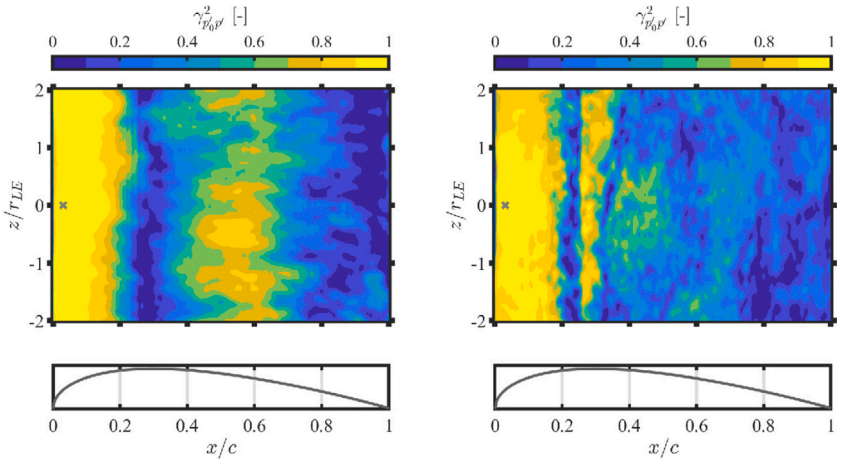

Fig. 5. Spatial-coherence contours of the pressure fluctuations on the surface of the solid (on the left) and porous (on the right) aerofoils at $St = 0.2$. The reference is set at the location $(x/r_{LE}; z/r_{LE}) = (0.47; 0)$, marked by the symbol x.

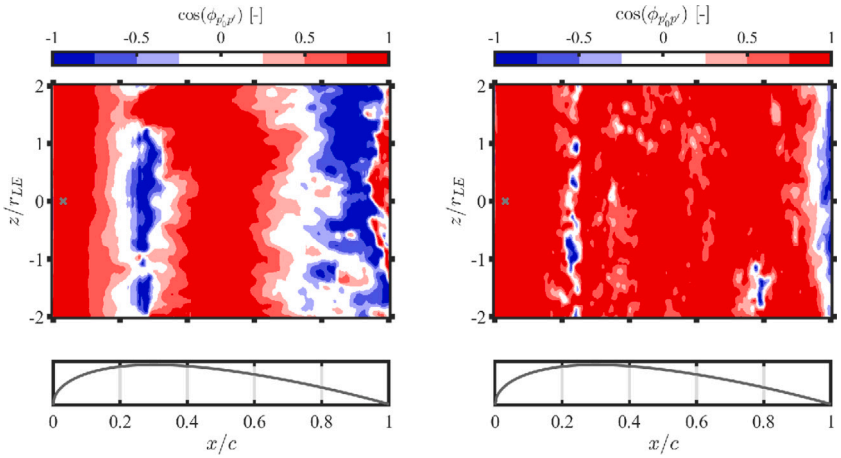

Fig. 6. Phase-difference contours of the pressure fluctuations expressed using the cosine function on the aerofoil surface at $St = 0.2$ for the solid (on the left) and porous (on the right) configurations. The reference is set at the location $(x/r_{LE}; z/r_{LE}) = (0.47; 0)$, marked by the symbol x.

configurations at the vortex-shedding frequency peak. The reference position is the same as in Fig. 3(b). Besides the strong spanwise correlation already described above, the results for the solid configuration show that $\gamma^2_{p'_0p'}$ is close to 1 over a distance of about $3\,r_{LE}$, or $0.2\,c$, from the leading edge. The present trend suggests that the region of the greatest curvature of the wing profile radiates in unison. Downstream of this location, the spatial coherence rapidly decreases, reaching approximately 0 around the position of maximum aerofoil thickness, and increases again at $0.4 < x/c < 0.6$. Porosity affects $\gamma^2_{p'_0p'}$ by slightly mitigating the initial high-coherence area. Both decay at $x/c > 0.2$ and increment at $0.4 < x/c < 0.6$ are also milder in this case. Furthermore, one major difference between the two configurations is that an area characterised by a relatively high spatial coherence abruptly appears in the surrounding of $x/c \approx 0.3$ for the porous wing profile. The origin behind this trend is still unclear but may be associated with the flow path within the porous material. Indeed, the incident fluid penetrates the aerofoil inner volume at the leading edge and is ejected at the position of maximum thickness [29], which corresponds to the region where $\gamma^2_{p'_0p'}$ increases. Additional investigations that are beyond the scope of the present paper would be required to elucidate this link.

In the regions where the spatial coherence of the surface-pressure fluctuations is high, the phase information of the cross-spectral densities can be evaluated to investigate potential interference effects. Fig. 6 depicts the phase-difference $\phi_{p'_0p'}$ contours of the unsteady pressures on the solid and porous aerofoil surfaces computed at the vortex-shedding frequency peak. Once again, the reference point is set at midspan of $x/r_{LE} = 0.47$. Following Kim et al. [53], data are plotted as $\cos\phi_{p'_0p'}$ so that the resulting values vary between 1 and -1 when the phase difference is 2 mπ rad (in phase) and $(2m+1)\pi$ rad (out of phase), respectively, m being an integer number. For both wing profiles, surface-pressure fluctuations are perfectly in phase in the region of greatest curvature of the NACA-0024 models, i.e. where $\gamma^2_{p'_0p'}$ is maximum. These conditions constitute the base for efficient sound production. At the location

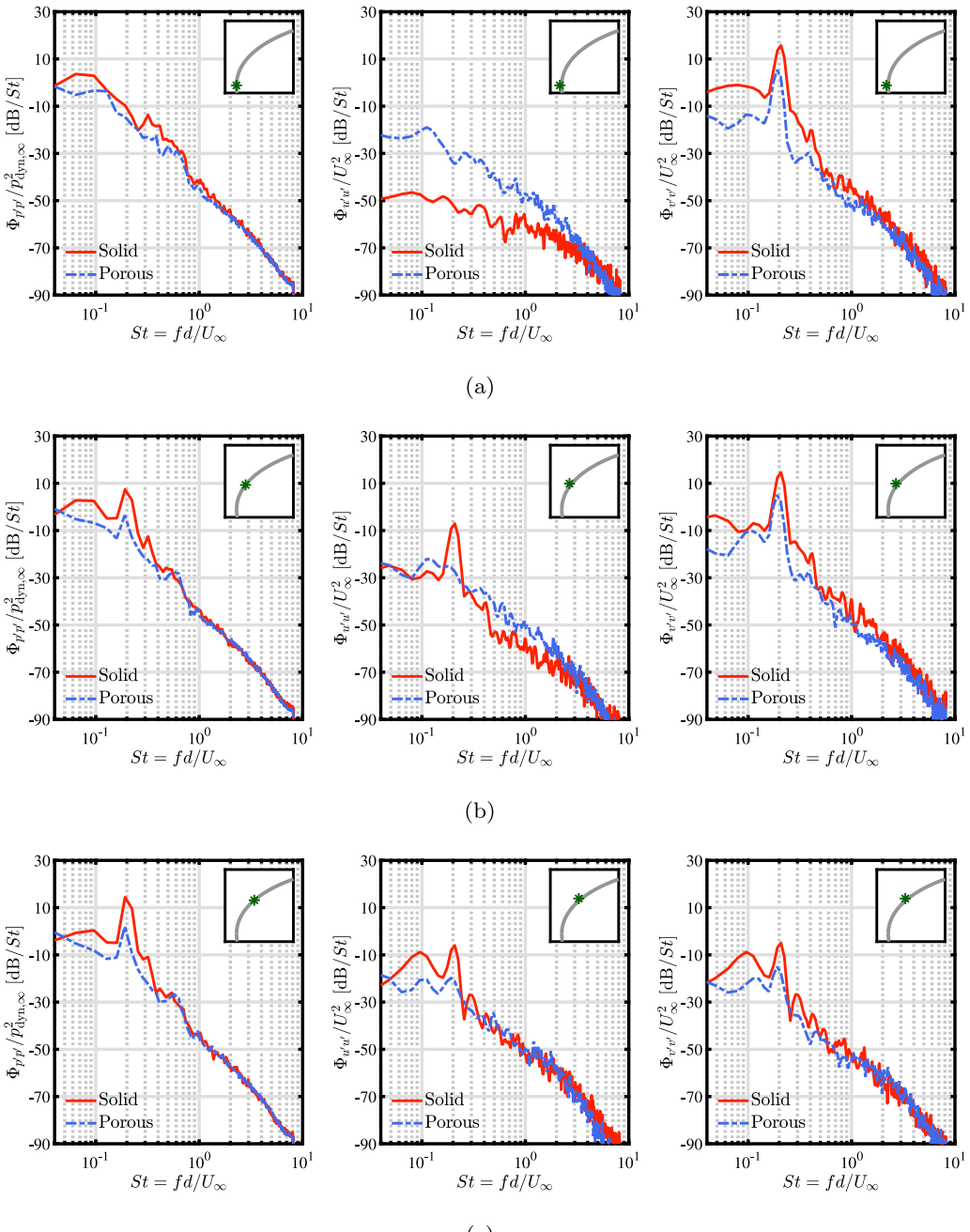

Fig. 7. Power spectral densities of the unsteady-pressure fluctuations (on the left) and the streamwise (in the centre) and upwash velocity fluctuations (on the right) for the solid and porous aerofoils averaged over the span. The pressures are extracted at (*a*) $x/r_{LE} = 0$, (*b*) $x/r_{LE} = 0.24$, and (*c*) $x/r_{LE} = 0.47$, whereas the velocities at a distance of $0.05\,r_{LE}$ from these locations considering the normal to the surface. The initial data are normalised by the corresponding free-stream values.

of maximum thickness of the aerofoil, the degree of destructive phase interference increases significantly for the impermeable configuration, in correspondence with the low-coherence area visible in Fig. 5. The same correlation between $\cos\phi_{p'_0p'} \approx -1$ and $\gamma^2_{p'_0p'} \approx 0$ is also found for the porous wing profile, for which the level of constructive phase interference is high throughout the entire surface.

A better insight into the physical mechanisms that induce the unsteady-pressure term is provided by evaluating the spectral content of the surface-pressure fluctuations and the turbulent velocities in the vicinity of the wing profiles. Such a comparison is reported in Fig. 7, where the power spectral densities of the quantities mentioned above are plotted for the solid and porous

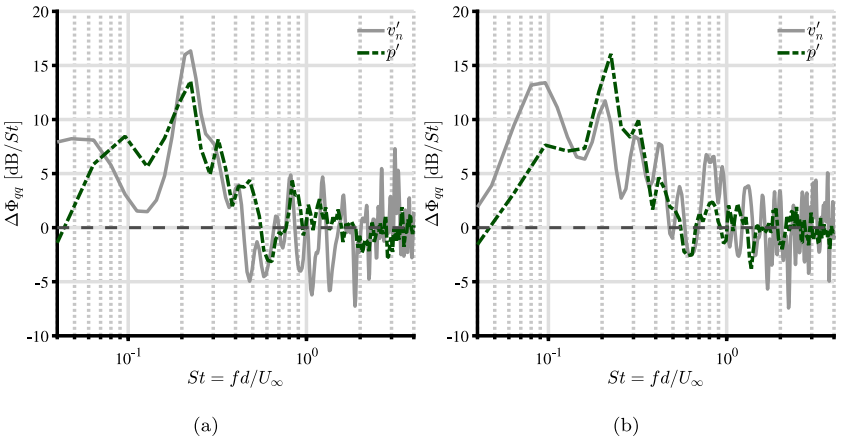

Fig. 8. Difference in the power spectral densities of the unsteady surface pressures and normal velocity fluctuations averaged over the span between the solid and porous aerofoils, where q is the generic term. The pressure is extracted at (*a*) $x/r_{LE} = 0.24$ and (*b*) $x/r_{LE} = 0.47$, whereas the velocity at a distance of $0.05\,r_{LE}$ normal to the surface from these locations.

aerofoils. Three chordwise positions ranging from the leading edge to the source peak are considered for the extraction of the surface-pressure data, namely $x/r_{LE} = 0$, $x/r_{LE} = 0.24$, and $x/r_{LE} = 0.47$. The corresponding locations at which velocity spectra are estimated lie at a distance of $0.05\,r_{LE}$ from the body considering the normal to the surface, by analogy with the analysis carried out by Zamponi et al. [30]. The power spectral densities are averaged over the span and normalised by U_∞^2 and $p_{\mathrm{dyn},\infty}^2$, such that the different quantities can be directly compared.

At the leading edge (Fig. 7(a)), $\Phi_{p'p'}$ and $\Phi_{u'u'}$ for both aerofoils do not exhibit any peak at $St = 0.2$, in contrast to $\Phi_{v'v'}$. The presence of porosity results in a mild attenuation in the pressure spectra at low frequencies and a reduction in the momentum transfer between the streamwise and upwash velocity fluctuations, which mitigates the decrease in u' and increase in v' from their upstream, undistorted values [30]. This is a consequence of the absence of the no-penetration condition at the porous wall and results in larger amplitudes of $\Phi_{u'u'}$ for the porous configuration with respect to the solid one. At $x/r_{LE} = 0.24$ (Fig. 7(b)), the vortex-shedding peak appears in the $\Phi_{p'p'}$ spectra for both configurations. A low-frequency attenuation is also present in this case due to the porous treatment of the wing profile. $\Phi_{u'u'}$ still features higher values for the porous aerofoil than for the solid one, yet with a minor discrepancy, and the peak at $St = 0.2$ is visible only for the latter. Likewise, the reduction in $\Phi_{v'v'}$ induced by porosity is lower. At $x/r_{LE} = 0.47$ (Fig. 7(c)), the results follow the trends discussed above. The vortex-shedding peak in the surface-pressure spectra is more evident, while the deviations between solid and porous configurations in the velocity spectra are further mitigated, leading to a comparable trend for the two components. Moreover, a slight shift of the vortex-shedding peak towards lower St occurs for all power spectral densities, in agreement with what has been seen in Fig. 4(b).

Interestingly, the frequency range at which porosity has an impact on the spectra is similar for $\Phi_{p'p'}$, $\Phi_{u'u'}$, and $\Phi_{v'v'}$. The results presented in Fig. 7 suggest that a potential link exists between the unsteady pressure on the surface and the nearby unsteady velocity u_n that is perpendicular to it, consistently with the analysis carried out by Panton and Linebarger [54]. Fig. 8 illustrates the relative power spectral densities of these two quantities, which are calculated as deviation between the solid and porous cases at $x/r_{LE} = 0.24$ and $x/r_{LE} = 0.47$. Positive values indicate a decrease in the spectra due to porosity, whereas negative ones denote an increase. For both locations, a notable agreement between $\Delta\Phi_{p'p'}$ and $\Delta\Phi_{u_n'u_n'}$ can be seen for most of the spectrum, which shows that the porous treatment reduces the power-spectral-density levels up to $St \approx 0.6$, with the maximum mitigation occurring at the vortex-shedding frequency. Nevertheless, such a scenario applies only partially to the results obtained at the leading edge. At this location, the normal $\boldsymbol{n}$ to the surface is parallel to the incoming flow. On the one hand, this correspondence would explain why the vortex-shedding frequency peak in the pressure spectra is not visible at the stagnation point, in accordance with the conclusions drawn on the spatial coherence in Fig. 3(a). On the other hand, the difference in $\Phi_{u'u'}$ due to porosity disagrees with the positive $\Delta\Phi_{p'p'}$ found in Fig. 7(a). One plausible explanation for this divergence relies on the fact that the unsteady surface pressure constitutes a less local quantity with respect to the velocity. Hence, at the leading edge, p' is affected by the pressures exerted on the surrounding region and is not solely determined by the upstream velocity fluctuations normal to the surface, also given the considerably higher amplitudes of $\Phi_{v'v'}$ when compared to $\Phi_{u'u'}$.

The considerations outlined above suggest that the physical mechanisms behind the turbulence-distortion attenuation proposed by Zamponi et al. [34] using the RDT are responsible for mitigating the pressure fluctuations on the aerofoil surface. In other words, porosity decreases the changes in the turbulent-flow field produced by the presence of the body and, in turn, the reaction force exerted by it due to unsteady incident velocity. This phenomenon constitutes the dominant noise-reduction mechanism of the porous treatment of the wing profile and confirms the hypotheses formulated in previous works [3,30,32,34].

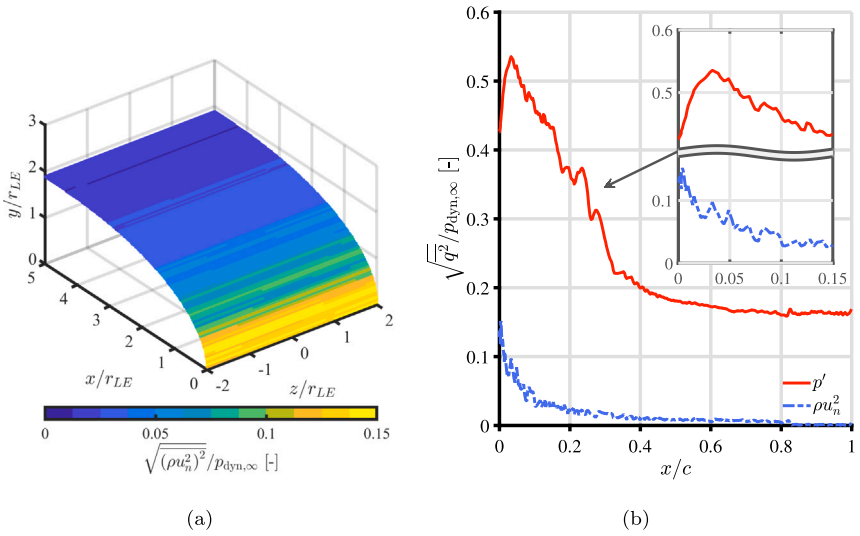

Fig. 9. (*a*) R.m.s. Reynolds-stresses ρu_n^2 contours on the porous aerofoil surface. (*b*) R.m.s. Reynolds-stresses ρu_n^2 and unsteady-pressure p' profiles averaged over the span of the porous aerofoil surface. q is the generic term. All terms are made dimensionless by the free-stream dynamic pressure.

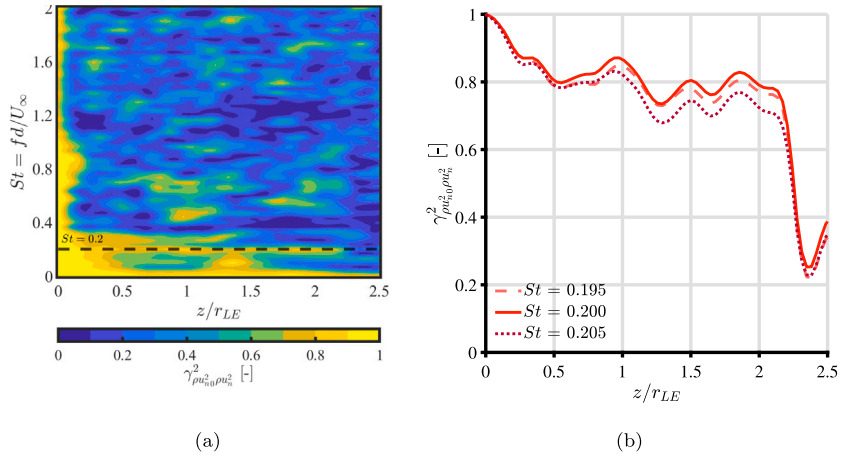

Fig. 10. (*a*) Spanwise spatial-coherence contours of the Reynolds stresses ρu_n^2 on the surface of the porous aerofoil computed at $x/r_{LE} = 0.06$. (*b*) Spanwise spatial-coherence profiles of ρu_n^2 on the surface of the porous aerofoil computed at $x/r_{LE} = 0.06$ for different interpolated Strouhal numbers in the vicinity of the vortex-shedding frequency peak. The reference is set at the midspan location ($z/r_{LE} = 0$).

5.2. Reynolds-stresses term

The presence of a transpiration velocity at the surface of the porous aerofoil implies that non-zero Reynolds stresses appear on it. According to Eq. (8), the far-field acoustic pressure associated with this source has a dipolar nature, and its relative contribution to the overall noise emitted by a porous wing profile has not been addressed in the literature. The investigation of the amplitude and correlation of the Reynolds-stresses term can shed light upon this influence and constitutes the topic of the present section. In the analyses performed below, the vector $\rho u_n \boldsymbol{u}$ from Eq. (8) is projected along the normal to the body to allow for a direct comparison with the surface-pressure fluctuations.

The rate of airflow penetrating the wing profile substantially affects the Reynolds-stresses term's magnitude, which is thus expected to be maximum in the stagnation region. This supposition is verified by the normalised r.m.s. contours of ρu_n^2 on the porous aerofoil surface depicted in Fig. 9(a), which highlights that the source peak is located close to the leading edge, at $x/r_{LE} \approx 0.06$, and rapidly decreases with the increasing chordwise position. However, its amplitude is considerably smaller than that of the unsteady-pressure term. Fig. 9(b) compares r.m.s. profiles for ρu_n^2 and p' averaged along the aerofoil span and provides a visualisation of this difference. The results show that the peak in p' amounts to approximately three times the peak in ρu_n^2. Moreover, the Reynolds-stresses term decays faster than the unsteady-pressure one, becoming negligible for $x/c > 0.1$.

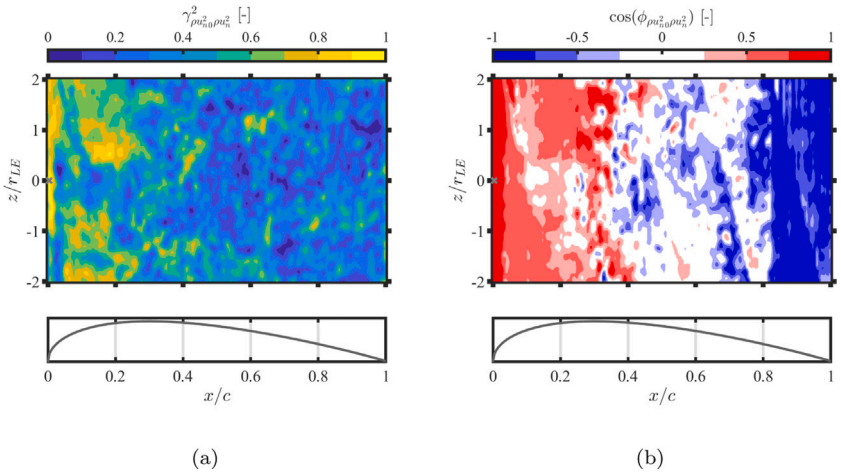

Fig. 11. (*a*) Spatial-coherence and (*b*) phase-difference (expressed with the cosine function) contours of the Reynolds stresses ρu_n^2 on the surface of the porous aerofoil at $St = 0.2$. The reference is set at the location $(x/r_{LE}; z/r_{LE}) = (0.06; 0)$, marked by the symbol x.

By analogy with the studies presented in Section 5.1, the acoustic efficiency of the noise source associated with ρu_n^2 can be investigated by looking at the spanwise spatial coherence in Fig. 10(a). In this case, $\gamma^2_{\rho u_{n0}^2 \rho u_n^2}$ is evaluated at the location where the maximum r.m.s. values of the Reynolds stresses occur, i.e. $x/r_{LE} \approx 0.06$, with a reference set at the aerofoil midspan. Once again, a clear peak at the vortex-shedding frequency appears, yet with a lower intensity and extension than for the surface-pressure fluctuations, as visible in the corresponding $\gamma^2_{\rho u_{n0}^2 \rho u_n^2}$ profiles extracted for $0.195 < St < 0.205$ in Fig. 10(b). These trends show that an abrupt loss of spatial coherence is found at a distance of about $2\,r_{LE}$ from the midspan, independently of the considered Strouhal number.

Furthermore, a relatively poor correlation is maintained with the sources downstream of the peak position. Fig. 11(a) illustrates the spatial coherence of ρu_n^2 computed at $St = 0.2$ along the porous aerofoil surface. The reference location is consistent with that of Fig. 10. The results reveal that the region of high $\gamma^2_{\rho u_{n0}^2 \rho u_n^2}$ is concentrated near the leading edge, where the transpiration velocity is larger. For $x/c > 0.3$, the correlation becomes negligible. Similar conclusions can be drawn for the corresponding phase difference reported in Fig. 11(b), which are once again calculated considering a reference at $(x/r_{LE}; z/r_{LE}) = (0.06; 0)$. In this case, the noise sources in the stagnation region are in phase and expected to radiate in unison, whereas those downstream of the maximum aerofoil thickness most likely do not contribute to the overall noise, also considering the much lower amplitudes reported in Fig. 9.

5.3. Correlation between unsteady-pressure and Reynolds-stresses terms

Despite the minor strength and source correlation of the Reynolds-stresses term with respect to the unsteady-pressure one, the former can potentially interfere constructively with the latter and increase the overall noise emitted by the porous aerofoil. This scenario is particularly relevant in the stagnation region, where the largest Reynolds stresses occur. In Fig. 12(a), the local coherence profile of p' and ρu_n^2 computed at $x/r_{LE} = 0.06$ and averaged along the span is depicted. Differently from the analyses carried out above, this quantity does not indicate a correlation between one variable evaluated at different points in space but rather between different variables calculated at the same point. Therefore, no reference location has to be defined. In the low-frequency range, $\gamma^2_{p' \rho u_n^2}$ varies between 0.2 and 0.6, with a steep increase up to 0.8 in correspondence with the vortex-shedding peak. For $St > 0.5$, the coherence stabilises just below 0.4, hence highlighting a partial correlation between the two terms at this position for the whole spectrum. In addition, the phase-difference profiles in Fig. 12(b) show that p' and ρu_n^2 are perfectly in phase up to $St \approx 1$, suggesting a strong constructive interference in the noise radiations. Above this Strouhal number, the phase starts slightly diverging, with $\cos(\phi_{p' \rho u_n^2})$ tending to 0.75.

Rather similar trends are found at more downstream locations. Figs. 12(c) and 12(d) depict the coherence and phase-difference profiles of the unsteady-pressure and Reynolds-stresses terms calculated at the position of maximum r.m.s. pressure, i.e. at $x/r_{LE} = 0.47$, respectively. Likewise, p' and ρu_n^2 feature significant correlation over the entire St spectrum but with lower amplitudes with respect to the leading-edge region (Fig. 12(c)). In particular, $\gamma^2_{p' \rho u_n^2}$ reduces approximately to 0.5 at the vortex-shedding peak and 0.3 in the high-St range. Furthermore, the two terms are still relatively in phase for $0.1 < St < 0.6$, whereas $\cos(\phi_{p' \rho u_n^2})$ oscillates around 0.5 elsewhere (Fig. 12(d)).

The high degree of correlation between p' and ρu_n^2 at the vortex-shedding frequency extends over the entire front region of the porous wing profile. In Fig. 13(a), the coherence of the two terms is calculated for the whole aerofoil surface at $St = 0.2$. $\gamma^2_{p' \rho u_n^2}$ ranges from 0.6 to 1 for $0 < x/c < 0.2$ and consistently decreases below 0.5 for larger chordwise positions. Moreover, as shown in the corresponding phase-difference contours in Fig. 13(b), the area of higher coherence is characterised by an in-phase behaviour,

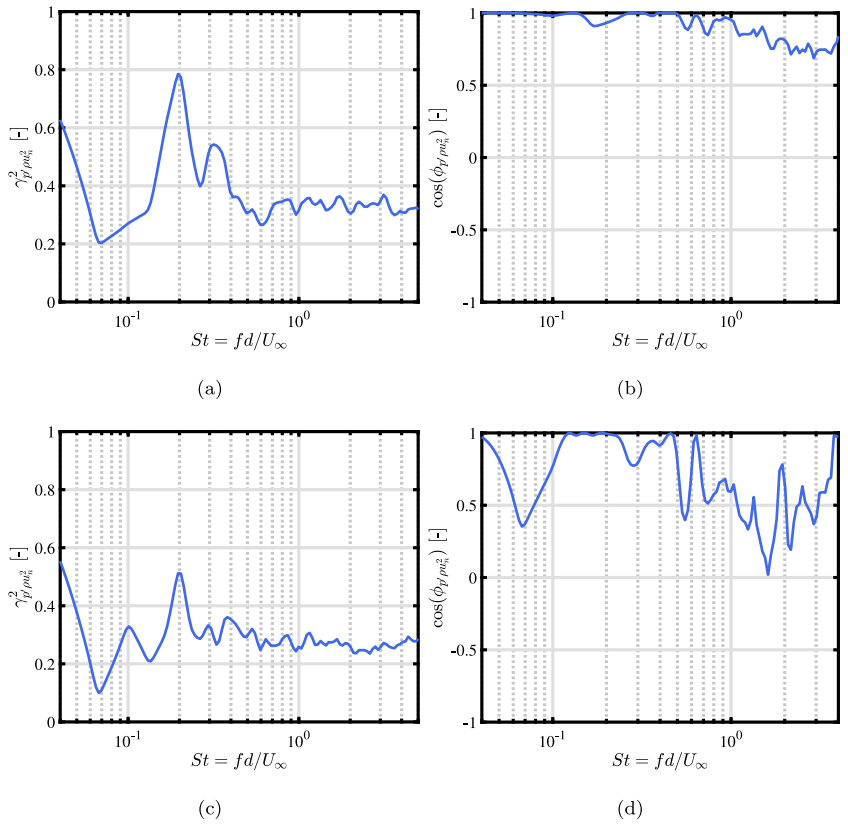

Fig. 12. Coherence (on the left) and phase-difference (on the right) profiles of the unsteady-pressure and Reynolds-stresses terms at $(a)-(b)$ $x/r_{LE} = 0.06$ and $(c)-(d)$ $x/r_{LE} = 0.47$ for the porous aerofoil averaged along the span.

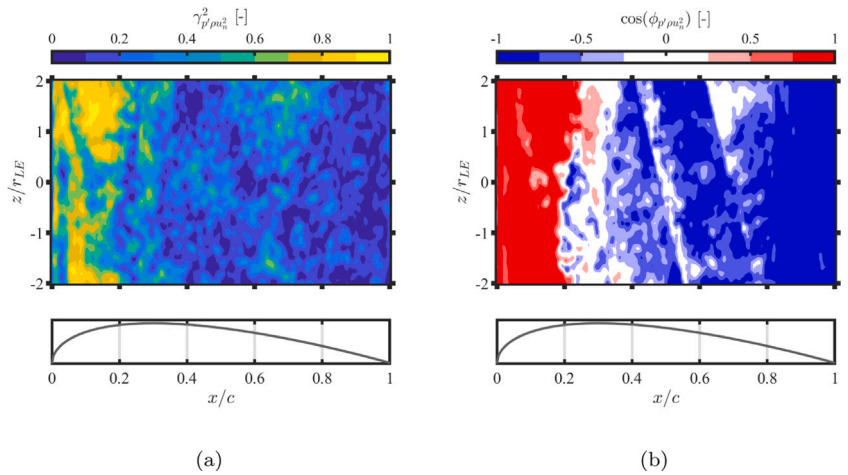

Fig. 13. (a) Coherence and (b) phase-difference (expressed with the cosine function) contours between the unsteady-pressure and Reynolds-stresses terms on the surface of the porous aerofoil at $St = 0.2$.

with $\cos(\phi_{p'\rho u_n^2}) \approx 1$, bearing similarities with the spatial-coherence trends of the unsteady-pressure and Reynolds-stresses terms analysed in Figs. 6 and 11. Therefore, the constructive interference between p' and ρu_n^2 hinted above is expected to occur in the whole region where the latter term is significant.

The mutual influence of the unsteady-pressure and Reynolds-stresses terms on the far-field acoustic pressure p^* is now discussed. The results of the integration of Curle dipolar sources on the acoustically-compact chordwise-varying patches described in Section 4.4.2 are reported in Fig. 14 for the solid and porous aerofoils. With regards to the coordinate reference system indicated

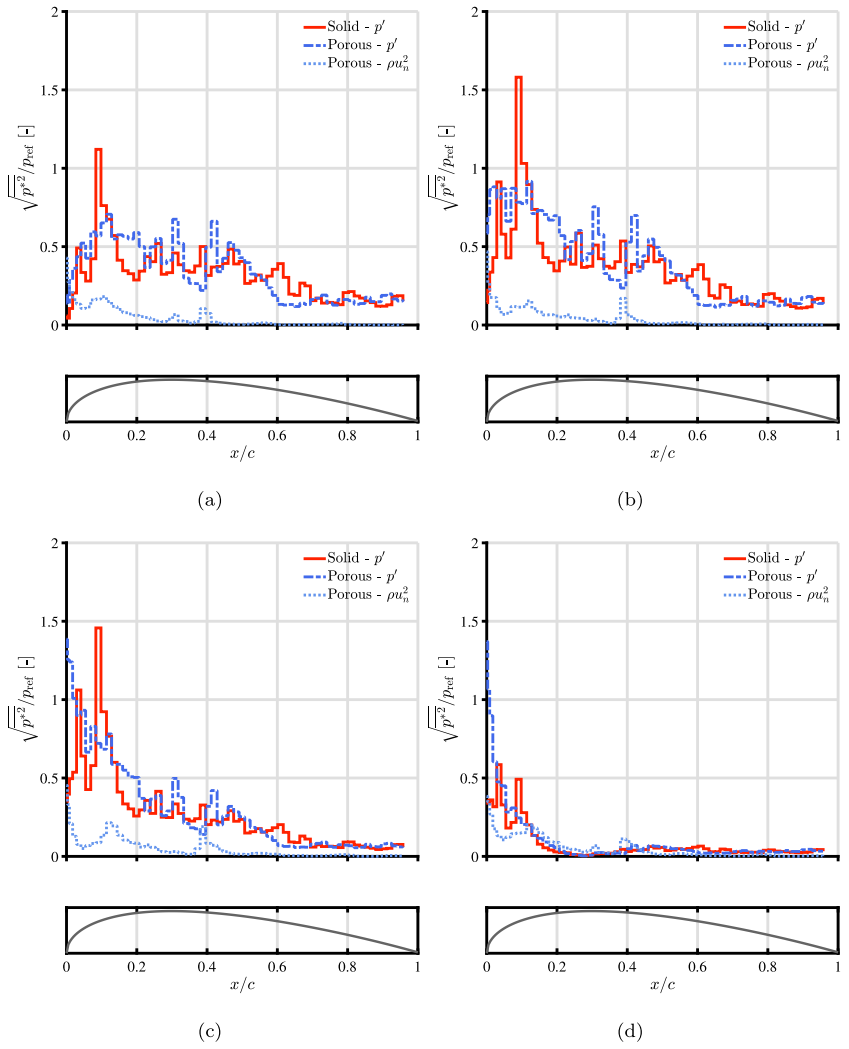

Fig. 14. Contributions of the unsteady-pressure and Reynolds-stresses terms to the r.m.s. far-field acoustic pressure emitted by different chordwise patches that are distributed along the solid and porous aerofoil surfaces. The listener is located at $R = 10\,c$ from the centre of the reference system, at (*a*) $\Theta = 60°$, (*b*) $\Theta = 90°$, (*c*) $\Theta = 135°$, and (*d*) $\Theta = 180°$ with respect to Fig. 1(a). All terms are normalised by the reference sound pressure $p_{\text{ref}} = 20\,\mu\text{Pa}$.

in Fig. 1(a), four different listener locations at a distance of $R = 10\,c$ from the body have been considered for the calculation, with Θ ranging from 60° to 180°. For each chordwise-varying patch, the corresponding r.m.s. value of p^* radiated due to the dipolar sources is plotted. The resulting quantities are non-dimensionalised with the acoustic reference pressure, i.e. $p_{\text{ref}} = 20\,\mu\text{Pa}$.

The results indicate that, in parallel with reducing noise, porosity shifts the dominant source regions. At $\Theta = 60°$ (Fig. 14(a)), the peak in p^* for the solid configuration occurs for the patch at $x/c \approx 0.08$, corresponding to $x/r_{LE} \approx 1.31$, hence downstream of the location of largest r.m.s. pressure fluctuations. For the porous one, the acoustic pressure features a slightly attenuated peak but larger contributions generated by the downstream patches, reflecting the trend shown in Fig. 2.

Comparing the different sources, the regions where the surface-pressure fluctuations and Reynolds stresses dominate the sound radiation are not the same either. Consistently with Fig. 9, the maximum acoustic pressure produced by the Reynolds-stresses term originates from the stagnation region, where it dominates over the unsteady-pressure term, and rapidly decreases downstream. The trends outlined above are even more emphasised for $\Theta = 90°$ (Fig. 14(b)) and $\Theta = 135°$ (Fig. 14(c)). In these cases, the integration of the term connected with p' results in larger p^* for both aerofoils in the region of greatest curvature, and the contribution of the Reynolds-stresses term is negligible throughout the entire porous wing profile. Moreover, for the solid configuration, a second peak in the unsteady-pressure term appears at approximately the location of the largest surface-pressure fluctuations, i.e. at $x/c \approx 0.03$.

The scenario considerably changes when approaching the stagnation streamline. At $\Theta = 180°$ (Fig. 14(d)), porosity yields no significant attenuation in the acoustic pressure generated by the unsteady-pressure term, which is considerably lower than for the previous observation angles. In contrast, p^* produced by the Reynolds-stresses term is higher for this listener position. As a result, the two dipolar sources for the porous surface patches in the stagnation region provide a similar contribution to the far-field acoustic

pressure. This trend is expected to increase the overall noise radiated by the porous wing profile due to their partial correlation highlighted in Fig. 12.

At this point, integrating the two terms on the entire solid and porous aerofoil surfaces could shed light upon the mutual interference of the different patches along the chord. It could also reveal the directivity pattern of the equivalent source associated with $\rho u_i u_j$, which potentially differs from that linked to p'. Indeed, according to Eq. (8), the direction of the dipole resulting from the Reynolds-stresses term is determined by the relative weights of the different components of the stress tensor and is unknown a priori. As a consequence, the additional sound sources induced by the non-zero Reynolds stresses at the flow-permeable surface might contribute to the radiated noise for directivity angles around the stagnation streamline, where the dipolar sound emissions produced by the unsteady-pressure term typically cancel out.

Nevertheless, Eq. (8) is only valid for compact sources. On the one hand, the hypothesis of acoustic compactness prevents the mathematical formulation used to integrate the different terms of Curle's analogy from being directly applied to the whole wing profile in the total frequency range of analysis, as pointed out in Section 4.4.2. On the other hand, it does not limit the validity of the discussions on the amplitude and phase of the equivalent sources outlined above. Indeed, the NACA-0024 aerofoil in this work can be safely assumed to be acoustically compact for most frequencies where turbulence-interaction noise is prominent. In particular, $\lambda/c \approx 7.3$ at the vortex-shedding peak. A possible extension of the mathematical model to non-compact sources would additionally enable the evaluation of high-frequency effects and the contributions from the monopolar term due to unsteady flow injection. These research questions will be addressed in future investigations.

Finally, the melamine foam considered in this study is characterised by lower static permeability than the 3D-printed materials or regularly perforated plates typically integrated into aerofoils for leading-edge noise mitigation [8,20]. Consequently, a less resistive flow-permeable medium would experience a larger transpiration velocity at the surface, which would, in turn, increase the relevance of the Reynolds-stresses term in the noise radiated by the porous wing profile.

6. Concluding remarks: effective porous-aerofoil design

The present research aims to evaluate the impact of porosity on the noise sources generated on the surface of a thick aerofoil interacting with incoming turbulence. When a porous body is considered in the formulation of Curle's analogy for a compact source region, an equivalent dipolar source associated with the unsteady Reynolds stresses appears in addition to the dipole related to the surface-pressure fluctuations. Both terms have been investigated through validated LES of solid and porous NACA-0024 profiles immersed in the wake of an upstream circular rod at a Reynolds number based on the cylinder diameter of $Re_d = 4.1 \times 10^4$.

The results show that the maximum r.m.s. pressure fluctuations on the aerofoil surface occur in the region of the greatest curvature, possibly due to the accelerating flow that makes the advected turbulent structures interact with the body at higher velocities. Porosity notably decreases their peak amplitude but spreads them over a larger downstream region. The analysis of the spatial coherence and phase difference reveals that, downstream of the leading edge, the pressure fluctuations maintain a high degree of correlation and in-phase behaviour throughout the span for both aerofoils at $St = 0.2$. This trend extends up to the 20% of the chord, suggesting that the region of the greatest curvature of the aerofoil radiates in unison. Additionally, a slight shift in the vortex-shedding frequency peak is found for the porous configuration, possibly linked to a change in the blockage exerted by the wing profile. The spectral content of the surface-pressure fluctuations indicates that the softened distortion experienced by turbulence in the vicinity of the porous surface also causes attenuation in the unsteady pressures. A remarkable agreement is found between the decrease in the power spectral densities of the pressure fluctuations on the surface and the normal component of the turbulent velocity close to it. This critical finding further confirms the hypotheses on the role of turbulence distortion in the leading-edge noise mitigation due to porosity formed in previous works.

The Reynolds-stresses term on the surface is found to be more relevant in the stagnation region of the wing profile, where the transpiration velocity is larger. Downstream of the 10% of the chord, they become negligible. Likewise, they maintain a high degree of correlation and in-phase behaviour at the vortex-shedding frequency peak. Despite their r.m.s. amplitude being considerably smaller than the unsteady-pressure term, mainly due to the low static permeability of the melamine foam, a partial correlation between the two sources is present in the entire front region of the porous wing profile, highlighting constructive interference, particularly at the vortex-shedding frequency. Curle's dipolar sources are subsequently integrated over chordwise-varying patches on the surface of the aerofoils for different listener positions. These patches can be considered acoustically compact in the frequency range of interest, in agreement with the assumptions upon which the formulation presented in the paper rests. The results demonstrate that the unsteady-pressure and Reynolds-stresses terms on the porous surface make a comparable contribution to the far-field acoustic pressure for a listener located near the stagnation streamline, decreasing the effectiveness of the porous treatment. The relevance of this outcome relies on the fact that the directivity pattern of the equivalent source connected with $\rho u_i u_j$ depends on the relative magnitude of the stress-tensor components and, therefore, may differ from that of the equivalent source linked to p'.

The conclusions of this analysis provide valuable insight into the design of porous wing profiles for turbulence-interaction noise reduction in a rod-aerofoil configuration. In this regard, the following observations can be made.

- The possibility of the flow permeating the inner volume of the aerofoil does not affect the unsteady pressures at the leading edge but attenuates the fluctuations just downstream of it. Porosity could be confined to this region, possibly limiting the aerodynamic performance loss typically linked to this passive noise-mitigation strategy that leads to a decrease in lift and an increase in drag.

- A uniform porous medium is ineffective in breaking the spanwise coherence or the in-phase behaviour of the surface-pressure fluctuations at the vortex-shedding frequency. A spanwise-varying distribution of pores could achieve this objective through a mechanism similar to that induced by leading-edge serrations, as proposed by Ayton et al. [27].
- Reducing the velocity fluctuations, i.e. mitigating the turbulence distortion, in the vicinity of the aerofoil results in a decrease in the unsteady pressure on its surface. This effect is produced by the milder reaction exerted by the wing profile and can be maximised using a more permeable medium [34] in specific locations to the potential detriment of the aerodynamic performance in terms of lift-force production.
- Non-zero Reynolds stresses at the surface of the porous aerofoil generate additional dipolar sources that contribute to the overall far-field noise and potentially diminish the sound mitigation, especially for materials with high static permeability. Preventing the flow from permeating the surface at the leading edge could counteract this effect and the possible deterioration in lift force associated with it.

It should be reminded that these considerations have been deduced from results obtained for a relatively thick wing profile. A thinner aerofoil may exhibit different contributions of the unsteady-pressure and Reynolds-stresses terms. Nevertheless, the authors believe that the deeper understanding gained in this work will be instrumental in assessing and improving the potential of advanced porous materials for noise reduction in industrial applications.

CRediT authorship contribution statement

R. Zamponi: Conceptualization, Methodology, Software, Validation, Formal analysis, Investigation, Data curation,Writing – original draft. **S. Satcunanathan:** Methodology, Software, Formal analysis, Data curation, Writing – original draft. **S. Moreau:** Conceptualization, Methodology, Writing – review & editing. **M. Meinke:** Supervision, Writing – review & editing. **W. Schröder:** Supervision, Writing – review & editing. **C. Schram:** Methodology, Visualization, Supervision, Writing – review & editing, Funding acquisition.

Data availability

Data will be made available on request.

Acknowledgements

This work is part of the ENODISE project and has received funding from the European Union's Horizon 2020 research and innovation programme under grant agreement No. 860103. Furthermore, the authors gratefully acknowledge the Gauss Centre for Supercomputing e.V. (www.gauss-centre.eu) for providing computing time on the GCS Supercomputer HAWK at Höchstleistungsrechenzentrum Stuttgart (www.hlrs.de) and S. Tamaro for helping with the integration of Curle's dipolar sources on the surfaces of the aerofoils.

References

[1] S. Kaji, T. Okazaki, Generation of sound by rotor-stator interaction, J. Sound Vib. 13 (3) (1970) 281–307, http://dx.doi.org/10.1016/S0022-460X(70)80020-7.
[2] S. Moreau, Turbomachinery noise predictions: Present and future, Acoustics 1 (2019) 92, http://dx.doi.org/10.3390/acoustics1010008.
[3] R. Zamponi, Investigation of Turbulence-Surface Interaction Noise Mechanisms and Their Reduction Using Porous Materials (Ph.D. thesis), Delft University of Technology, 2021, http://dx.doi.org/10.4233/uuid:d332c7e3-87be-4ed6-aa71-e629ef77e07a.
[4] M.E. Goldstein, Unsteady vortical and entropic distortions of potential flows round arbitrary obstacles, J. Fluid Mech. 89 (1978) 433, http://dx.doi.org/10.1017/S0022112078002682.
[5] M.J. Lighthill, On sound generated aerodynamically i. general theory, Proc. R. Soc. London. Ser. A 211 (1107) (1952) 564–587, http://dx.doi.org/10.1098/rspa.1952.0060.
[6] N. Curle, The influence of solid boundaries upon aerodynamic sound, Proc. R. Soc. London. Ser. A 231 (1187) (1955) 505–514, http://dx.doi.org/10.1098/rspa.1955.0191.
[7] S. Lee, Reduction of blade-vortex interaction noise through porous leading edge, AIAA J. 32 (3) (1994) 480–488, http://dx.doi.org/10.2514/3.12011.
[8] T. Geyer, E. Sarradj, J. Giesler, M. Hobracht, Experimental assessment of the noise generated at the leading edge of porous airfoils using microphone array techniques, in: 17th AIAA/CEAS Aeroacoustics Conference (32nd AIAA Aeroacoustics Conference), American Institute of Aeronautics and Astronautics, Portland, Oregon, 2011, http://dx.doi.org/10.2514/6.2011-2713.
[9] T. Geyer, E. Sarradj, J. Giesler, Application of a beamforming technique to the measurement of airfoil leading edge noise, Adv. Acoust. Vib. 2012 (2012) 1–16, http://dx.doi.org/10.1155/2012/905461.
[10] E. Sarradj, T. Geyer, Symbolic regression modeling of noise generation at porous airfoils, J. Sound Vib. 333 (14) (2014) 3189–3202, http://dx.doi.org/10.1016/j.jsv.2014.02.037.
[11] R.E. Mineck, P.M. Hartwich, Effect of Full-Chord Porosity on Aerodynamic Characteristics of the NACA 0012 Airfoil, Technical Publication NASA/TP-3591, 1996.
[12] E. Sarradj, T. Geyer, Noise generation by porous airfoils, in: 13th AIAA/CEAS Aeroacoustics Conference (28th AIAA Aeroacoustics Conference), American Institute of Aeronautics and Astronautics, Rome, Italy, 2007, http://dx.doi.org/10.2514/6.2007-3719.
[13] C. Teruna, F. Avallone, D. Casalino, D. Ragni, Numerical investigation of leading edge noise reduction on a rod-airfoil configuration using porous materials and serrations, J. Sound Vib. (2020) 115880, http://dx.doi.org/10.1016/j.jsv.2020.115880.
[14] T.F. Geyer, A. Lucius, M. Schrödter, M. Schneider, E. Sarradj, Reduction of turbulence interaction noise through airfoils with perforated leading edges, Acta Acust. United Acust. 105 (1) (2019) 109–122, http://dx.doi.org/10.3813/AAA.919292.

[15] S. Tamaro, R. Zamponi, C. Schram, Development of a didactic demonstrator for flow-induced noise mechanisms and mitigation technologies, J. Acoust. Soc. Am. 151 (2022) 898, http://dx.doi.org/10.1121/10.0009366.
[16] M. Roger, C. Schram, L. de Santana, Reduction of airfoil turbulence-impingement noise by means of leading-edge serrations and/or porous material, in: 19th AIAA/CEAS Aeroacoustics Conference, American Institute of Aeronautics and Astronautics, Berlin, Germany, 2013, http://dx.doi.org/10.2514/6.2013-2108.
[17] M. Roger, S. Moreau, Airfoil turbulence-impingement noise reduction by porosity or wavy leading-edge cut: Experimental investigations, in: 45th International Congress and Exposition on Noise Control Engineering, Institute of Noise Control Engineering, Hamburg, Germany, 2016, pp. 6366–6375.
[18] G. Bampanis, M. Roger, On the turbulence-impingement noise of a NACA-12 airfoil with porous inclusions, in: 26th AIAA/CEAS Aeroacoustics Conference, American Institute of Aeronautics and Astronautics, Virtual event, 2020, http://dx.doi.org/10.2514/6.2020-2577.
[19] C. Ocker, F. Czwielong, T.F. Geyer, P. Chaitanya, M. Merkel, S. Becker, Permeable structures for leading edge noise reduction, in: AIAA AVIATION 2021 FORUM, American Institute of Aeronautics and Astronautics, VIRTUAL EVENT, 2021, http://dx.doi.org/10.2514/6.2021-2192.
[20] C. Ocker, T.F. Geyer, F. Czwielong, F. Krömer, W. Pannert, M. Merkel, S. Becker, Permeable leading edges for airfoil and fan noise reduction in disturbed inflow, AIAA J. 59 (12) (2021) 4969–4986, http://dx.doi.org/10.2514/1.J060396.
[21] C. Paruchuri, P. Joseph, T.P. Chong, M. Priddin, L.J. Ayton, On the noise reduction mechanisms of porous aerofoil leading edges, J. Sound Vib. 485 (2020) 115574, http://dx.doi.org/10.1016/j.jsv.2020.115574.
[22] S. Palleja-Cabre, P. Chaitanya, P. Joseph, J.W. Kim, M.J. Priddin, L.J. Ayton, T.F. Geyer, T.P. Chong, Downstream porosity for the reduction of turbulence-aerofoil interaction noise, J. Sound Vib. (2022) 117324, http://dx.doi.org/10.1016/j.jsv.2022.117324.
[23] M.J. Priddin, L.J. Ayton, S. Palleja-Cabre, P. Chaitanya, P. Joseph, Downstream perforations for the reduction of turbulence-aerofoil interaction noise: Part II - theoretical investigation, in: AIAA AVIATION 2021 FORUM, American Institute of Aeronautics and Astronautics, VIRTUAL EVENT, 2021, http://dx.doi.org/10.2514/6.2021-2147.
[24] L.J. Ayton, M.J. Colbrook, T. Geyer, P. Chaitanya, E. Sarradj, Reducing aerofoil–turbulence interaction noise through chordwise-varying porosity, J. Fluid Mech. 906 (2021) A1, http://dx.doi.org/10.1017/jfm.2020.746.
[25] M. Roger, S. Moreau, Back-scattering correction and further extensions of Amiet's trailing-edge noise model. Part 1: theory, J. Sound Vib. 286 (3) (2005) 477–506, http://dx.doi.org/10.1016/j.jsv.2004.10.054.
[26] S. Moreau, M. Roger, Back-scattering correction and further extensions of Amiet's trailing-edge noise model. Part II: Application, J. Sound Vib. 323 (1–2) (2009) 397–425, http://dx.doi.org/10.1016/j.jsv.2008.11.051.
[27] L.J. Ayton, O. Karapiperis, M. Awasthi, D. Moreau, C.J. Doolan, Spanwise varying porosity for the enhancement of leading-edge noise reduction, in: AIAA AVIATION 2021 FORUM, http://dx.doi.org/10.2514/6.2021-2191.
[28] R. Zamponi, D. Ragni, N. Van de Wyer, C. Schram, Experimental investigation of airfoil turbulence-impingement noise reduction using porous treatment, in: 25th AIAA/CEAS Aeroacoustics Conference, American Institute of Aeronautics and Astronautics, Delft, The Netherlands, 2019, http://dx.doi.org/10.2514/6.2019-2649.
[29] S. Satcunanathan, M. Meinke, W. Schröder, Prediction of noise mitigation by porous media based on a direct-hybrid CFD/CAA method, in: 25th AIAA/CEAS Aeroacoustics Conference, American Institute of Aeronautics and Astronautics, Delft, The Netherlands, 2019, http://dx.doi.org/10.2514/6.2019-2696.
[30] R. Zamponi, S. Satcunanathan, S. Moreau, D. Ragni, M. Meinke, W. Schröder, C. Schram, On the role of turbulence distortion on leading-edge noise reduction by means of porosity, J. Sound Vib. 485 (2020) 115561, http://dx.doi.org/10.1016/j.jsv.2020.115561.
[31] R. Zamponi, S. Moreau, D. Ragni, C.F. Schram, Experimental and analytical investigation of the distortion of turbulence interacting with a porous airfoil, in: AIAA AVIATION 2021 FORUM, American Institute of Aeronautics and Astronautics, VIRTUAL EVENT, 2021, http://dx.doi.org/10.2514/6.2021-2289.
[32] S. Tamaro, R. Zamponi, D. Ragni, C. Teruna, C. Schram, Experimental investigation of turbulent coherent structures interacting with a porous airfoil, Exp. Fluids 62 (2021) 94, http://dx.doi.org/10.1007/s00348-021-03170-2.
[33] J.C.R. Hunt, A theory of turbulent flow round two-dimensional bluff bodies, J. Fluid Mech. 61 (4) (1973) 625–706, http://dx.doi.org/10.1017/S0022112073000893.
[34] R. Zamponi, S. Moreau, C. Schram, Rapid distortion theory of turbulent flow around a porous cylinder, J. Fluid Mech. 915 (2021) A27, http://dx.doi.org/10.1017/jfm.2021.8.
[35] S.A.L. Glegg, W. Devenport, Aeroacoustics of Low Mach Number Flows: Fundamentals, Analysis, and Measurement, Academic Press, London, 2017.
[36] M.E. Goldstein, Aeroacoustics, in: NASA SP, Scientific and Technical Information Office, National Aeronautics and Space Administration, 1974.
[37] S. Whitaker, The Method of Volume Averaging, in: Theory and Applications of Transport in Porous Media, vol. 13, Springer Netherlands, Dordrecht, 1999, http://dx.doi.org/10.1007/978-94-017-3389-2.
[38] W. Breugem, B. Boersma, R. Uittenbogaard, The influence of wall permeability on turbulent channel flow, J. Fluid Mech. 562 (2006) 35–72, http://dx.doi.org/10.1017/S0022112006000887.
[39] S. Whitaker, Flow in porous media I: A theoretical derivation of Darcy's law, Transp. Porous Media 1 (1986) 3–25, http://dx.doi.org/10.1007/BF01036523.
[40] S. Whitaker, The Forchheimer equation: A theoretical development, Transp. Porous Media 25 (1) (1996) 27–61, http://dx.doi.org/10.1007/BF00141261.
[41] L. Schneiders, D. Hartmann, M. Meinke, W. Schröder, An accurate moving boundary formulation in cut-cell methods, J. Comput. Phys. 235 (2013) 786–809, http://dx.doi.org/10.1016/j.jcp.2012.09.038.
[42] M.C. Jacob, J. Boudet, D. Casalino, M. Michard, A rod-airfoil experiment as a benchmark for broadband noise modeling, Theor. Comput. Fluid Dyn. 19 (3) (2005) 171–196, http://dx.doi.org/10.1007/s00162-004-0108-6.
[43] V. Lorenzoni, M. Tuinstra, F. Scarano, On the use of time-resolved particle image velocimetry for the investigation of rod–airfoil aeroacoustics, J. Sound Vib. 331 (23) (2012) 5012–5027, http://dx.doi.org/10.1016/j.jsv.2012.05.034.
[44] P. Batten, U. Goldberg, S. Chakravarthy, Interfacing statistical turbulence closures with large-Eddy simulation, AIAA J. 42 (3) (2004) 485–492, http://dx.doi.org/10.2514/1.3496.
[45] C. Bogey, C. Bailly, Effects of inflow conditions and forcing on subsonic jet flows and noise, AIAA J. 43 (5) (2005) 1000–1007, http://dx.doi.org/10.2514/1.7465.
[46] S. Satcunathan, R. Zamponi, M. Meinke, N. Van de Wyer, C. Schram, W. Schröder, Validation of a model for acoustic absorption in porous media, in: 48th International Congress and Exhibition on Noise Control Engineering, Institute of Noise Control Engineering, Madrid, Spain, 2019, pp. 4329–4344.
[47] P. Welch, The use of fast Fourier transform for the estimation of power spectra: A method based on time averaging over short, modified periodograms, IEEE Trans. Audio Electroacoust. 15 (2) (1967) 70–73, http://dx.doi.org/10.1109/TAU.1967.1161901.
[48] C. Schram, A boundary element extension of Curle's analogy for non-compact geometries at low-Mach numbers, J. Sound Vib. 322 (1–2) (2009) 264–281, http://dx.doi.org/10.1016/j.jsv.2008.11.011.
[49] R. Zamponi, S. Satcunanathan, S. Moreau, M. Meinke, W. Schroeder, C.F. Schram, Investigation of curle's dipolar sources on a porous airfoil interacting with incoming turbulence, in: 28th AIAA/CEAS Aeroacoustics 2022 Conference, American Institute of Aeronautics and Astronautics, Southampton, UK, 2022, http://dx.doi.org/10.2514/6.2022-2985.
[50] R.K. Amiet, Acoustic radiation from an airfoil in a turbulent stream, J. Sound Vib. 41 (4) (1975) 407–420, http://dx.doi.org/10.1016/S0022-460X(75)80105-2.
[51] H. Liu, M. Azarpeyvand, J. Wei, Z. Qu, Tandem cylinder aerodynamic sound control using porous coating, J. Sound Vib. 334 (2015) 190–201, http://dx.doi.org/10.1016/j.jsv.2014.09.013.

[52] H. Liu, Y. Wang, J. Wei, Z. Qu, The importance of controlling the upstream body wake in tandem cylinders system for noise reduction, Proc. Inst. Mech. Eng. G 232 (3) (2018) 517–531, http://dx.doi.org/10.1177/0954410016682271.
[53] J.W. Kim, S. Haeri, P.F. Joseph, On the reduction of aerofoil–turbulence interaction noise associated with wavy leading edges, J. Fluid Mech. 792 (2016) 526–552, http://dx.doi.org/10.1017/jfm.2016.95.
[54] R.L. Panton, J.H. Linebarger, Wall pressure spectra calculations for equilibrium boundary layers, J. Fluid Mech. 65 (2) (1974) 261–287, http://dx.doi.org/10.1017/S0022112074001388.